

Department of Physics and Astronomy
University of Heidelberg

Bachelor Thesis in Physics
submitted by

Jens Kröger

born in Lübbecke (Germany)

2014

**Data Transmission at High Rates
via Kapton Flexprints for the Mu3e Experiment**

This Bachelor Thesis has been carried out by
Jens Kröger

at the
Physikalisches Institut Heidelberg

under the supervision of
Prof. Dr. André Schöning

Abstract

The Mu3e experiment is aiming to search for the neutrinoless muon decay $\mu^+ \rightarrow e^+e^-e^+$ with a sensitivity of one in 10^{16} decays or better. This decay is lepton flavour violating and strongly suppressed within the Standard Model. Therefore, even a single decay signal would be a clear hint for new physics.

The concept of the Mu3e experiment is to achieve a very good momentum and time resolution and an excellent vertex reconstruction to suppress background to a sufficient level. Since the decay electrons have a low energy up to 53 MeV, multiple Coulomb scattering is the dominating limiting factor for the momentum and vertex resolution. Therefore, the material budget inside the detector region must be kept at a minimum. To achieve this, pixel detectors with a thickness of only 50 μm will be used which are carried by a Kapton foil support structure. The pixel detectors shall be linked to front-end FPGAs via ultra-thin Kapton flexprints.

The production and performance tests of self-manufactured Kapton flexprints are the main scope of this thesis. It has been shown that flexprints with a trace width of 120 μm and a trace separation of 110 μm can be manufactured reliably with a laser platform available at the Heidelberg University. In addition, bit error rate tests have been performed which resulted in bit error rates below $O(10^{-15})$ for 17 parallel channels at a transmission rate of 800 Mbit/s each. Moreover, eye diagrams have been analyzed to understand which factors mainly affect the signal quality.

Zusammenfassung

Das Mu3e-Experiment hat zum Ziel, den neutrinolosen Myon-Zerfall $\mu^+ \rightarrow e^+e^-e^+$ mit einer Genauigkeit von einem in 10^{16} Zerfällen oder besser zu suchen. Dieser Zerfall ist leptonzahlverletzend und damit im Standardmodell so stark unterdrückt, dass selbst ein einziger gemessener Zerfall ein klarer Hinweis auf neue Physik wäre.

Das Konzept des Mu3e-Experiments ist es, eine sehr gute Impuls- und Zeitauflösung und Vertexrekonstruktion zu erreichen, um den Untergrund ausreichend stark zu unterdrücken. Da die Zerfallselektronen eine niedrige Energie von bis zu 53 MeV haben, ist hauptsächlich Coulomb-Vielfachstreuung der limitierende Faktor für die Impuls- und Vertexauflösung. Deshalb soll innerhalb des Detektors so wenig Material wie möglich verbaut werden. Um dies zu erreichen, sollen Pixeldetektoren mit einer Dicke von lediglich 50 μm verwendet werden, die von einer Struktur aus Kaptonfolie getragen werden. Die Daten werden über ultradünne Kaptonflexprints zu Front-End FPGAs übertragen.

Die Herstellung sowie Performance-Tests selbsthergestellter Kapton-Flexprints sind die Schwerpunkte dieser Arbeit. Es konnte gezeigt werden, dass Flexprints mit Leiterbahnbreiten von 120 μm und Abständen von 110 μm zuverlässig mit einer Laserplattform an der Universität Heidelberg hergestellt werden können. Zusätzlich sind Fehlerraten-Tests durchgeführt worden, die Werte unter $O(10^{-15})$ für 17 parallele Kanäle bei einer Datenrate von je 800 Mbit/s ergeben haben. Darüber hinaus sind Augen-diagramme analysiert worden, um zu verstehen, welche Faktoren die Signalqualität im Wesentlichen beeinflussen.

Contents

I	Theory & Background	1
1	Theoretical Background	2
1.1	The Standard Model	2
1.1.1	The Elementary Particles	2
1.1.2	Muon Decays	3
1.2	Experimental Situation	4
2	The Mu3e Experiment	6
2.1	The Mu3e Experiment	6
2.1.1	The Signal Decay	6
2.1.2	Background Decays	7
2.1.3	Experimental Concept	8
2.1.4	The Readout Concept	10
2.1.5	The Muon Beam	11
3	Basics of Data Transmission	13
3.1	Signals	13
3.1.1	Low Voltage Differential Signaling	13
3.1.2	Data Encoding	15
3.2	Transmission Lines	18
3.2.1	The Characteristic Impedance	19
3.2.2	Microstrips	20
3.3	Signal Quality Checks	21
3.3.1	Bit Error Rate Tests (BERTs)	22
3.3.2	Eye Diagrams	23
II	Measurements & Results	25
4	Manufacturing of Kapton Flexprints	26
4.1	The Laser Platform	26
4.2	Kapton	27
4.2.1	Physical Properties	27
4.2.2	Electrical Properties	27
4.3	Aluminum	29
4.4	Structure Sizes	30
4.4.1	Impedance Calculations	30

4.4.2	Test Structures	31
4.5	Flexprint Cables	34
4.5.1	Limitations	35
4.5.2	Obtaining Different Types of Microstrips	37
4.5.3	Mechanical Properties	38
4.5.4	Blackening of the Kapton	39
5	Performance of BERTs	42
5.1	Hardware	43
5.1.1	Field Programmable Gate Array	43
5.1.2	FPGA Development Board	43
5.1.3	HSMC Flexprint Adapter Board	43
5.2	Software	45
5.2.1	Altera Quartus II	45
5.2.2	ModelSim	46
5.3	Firmware: BERT Implementation	46
5.3.1	Data Generator	46
5.3.2	8b/10b Encoder	47
5.3.3	LVDS Transmitter	47
5.3.4	LVDS Receiver	47
5.3.5	8b/10b Decoder	47
5.3.6	Data Checker	48
5.4	BERT Results	49
6	Analysis of Eye Diagrams	51
6.1	Test Setup	51
6.1.1	Tektronix DPO 7254C Digital Phosphor Oscilloscope	52
6.1.2	Tektronix TDP3500 Differential Probe	52
6.2	Eye Diagram Results	53
6.2.1	Influence of the HSMC Flexprint Adapter Board	53
6.2.2	Influence of the Cable Length	56
6.2.3	Influence of the Transmission Rate	59
6.2.4	Influence of the Pre-Emphasis	60
6.2.5	Crosstalk between Trace Pairs	61
6.2.6	Influence of the Microstrip Type	62
6.2.7	Influence of the Knee Length	64
III	Conclusion & Outlook	67
7	Conclusion	68
7.1	Manufacturing of Kapton Flexprints	68
7.2	BERT Results	69
7.3	Eye Diagram Results	69
7.4	Recommendations	70

8 Outlook	71
8.1 Consequences for the Mu3e Experiment	71
8.1.1 Spatial Constraints	71
8.1.2 Transmission Errors	72
8.2 Further Work	73
List of Figures	74
List of Tables	75
Bibliography	76
Acknowledgements	80

Part I

Theory & Background

1 Theoretical Background

1.1 The Standard Model

1.1.1 The Elementary Particles

The Standard Model of particle physics (SM) [1] is a quantum field theory that comprises the description of the smallest constituents of matter, the elementary particles, as well as the electromagnetic, the weak, and the strong interaction. Only gravity cannot be described. The SM was developed throughout the second half of the 20th century and has passed countless experimental tests until today. Especially the recent discovery of a new particle, which is likely to be the long predicted Higgs boson, has given further support to this theory [2, 3].

According to the SM, the fundamental particles comprise six quarks, six leptons, and their corresponding anti-particles. Furthermore, there are four types of gauge bosons and the Higgs boson (see Figure 1.1). The quarks and leptons form three generations. The first generation contains the up quark (u) and the down quark (d) with charges of $+2/3$ and $-1/3$ in units of the elementary charge, the electron (e^-) and the electrically neutral electron neutrino (ν_e).

The second and the third generation are also made up of a pair of quarks, a lepton and a neutrino. These are the charm quark (c) and the strange quark (s) together with the muon (μ^-) and the muon neutrino (ν_μ) in the second generation and the top quark (t), the bottom quark (b) together with the tau (τ) and the tau neutrino (ν_τ) in the third generation.

All quarks and leptons are spin $1/2$ particles, i.e. they are fermions. The interaction between them is mediated by the gauge bosons which have spin 1. The eight gluons are responsible for the strong interaction, the photon (γ) mediates the electromagnetic force and the Z^0 , W^+ and W^- go with the weak interaction.

In the SM, the neutrinos are considered to be massless. The so-called lepton flavour number, i.e. the number of anti-leptons subtracted from the number of leptons of one generation, is a conserved quantity.

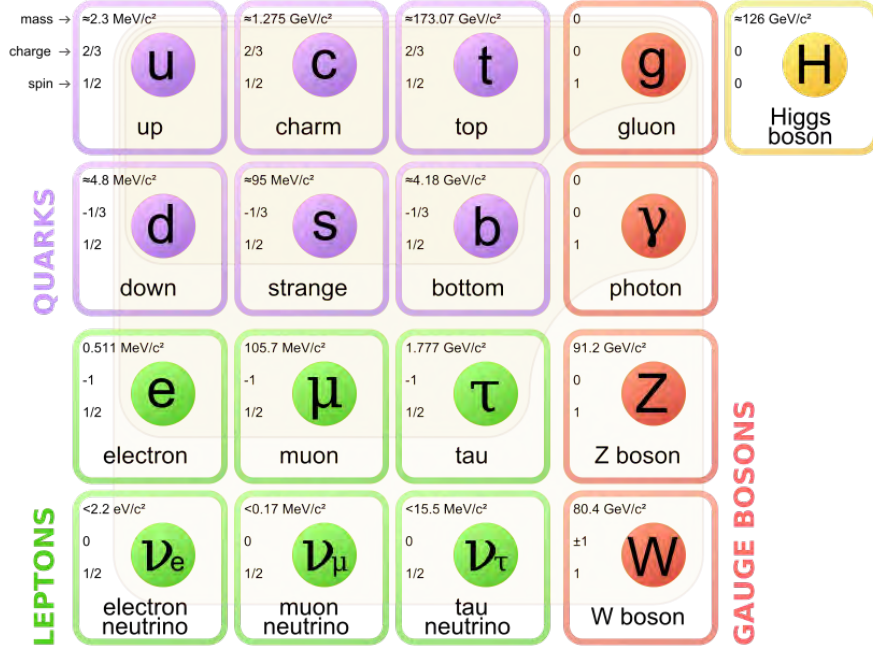
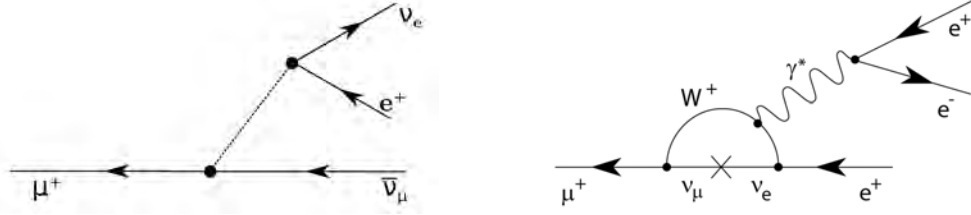


Figure 1.1: Particles described by the SM [4].

In spite of the great successes of the SM, observations have been made which cannot be explained by this theory. Several experiments have observed neutrino oscillation, such as Super-Kamiokande [5], SNO [6], KamLAND [7], and Daya-Bay [8]. To explain this mixing of the flavour eigenstates, the neutrinos need a non-vanishing mass, which is not foreseen in the SM. An extension by heavy right-handed neutrinos, called ν SM, yields consistent results with oscillation experiments [9]. Still it cannot be explained why the neutrino masses are orders of magnitude smaller than those of the other particles. Moreover, ν SM does not provide any explanation for the observed matter-antimatter-asymmetry, the origin of dark matter, or the existence three generations of particles. These phenomena motivate theories beyond the Standard Model (BSM), such as supersymmetric theories (SUSY). In contrast to the SM, many of these predict flavour violating processes at an observable branching ratio.

1.1.2 Muon Decays

(Anti-)muons are unstable and have a mean lifetime of about $2.2 \mu\text{s}$. The dominating decay in the SM is $\mu^+ \rightarrow e^+ \nu_e \bar{\nu}_\mu$ [1]. Considering neutrino mixing (and therefore allowing lepton flavour violation) the muon decay can also be realised without outgoing neutrinos (see Figure 1.2b).

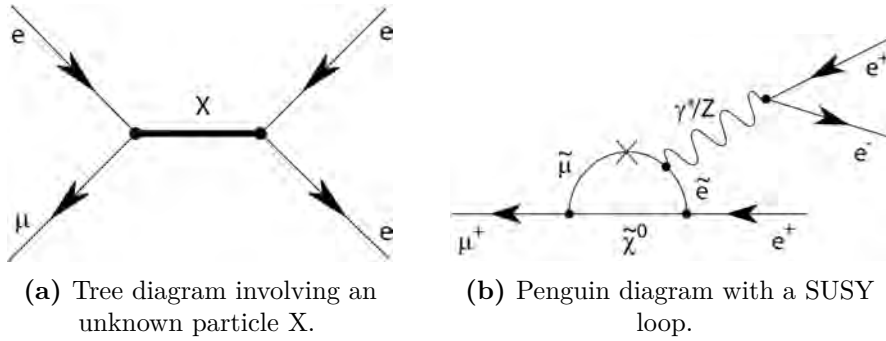


(a) Dominant SM muon decay: the Michel decay. (b) Strongly suppressed decay $\mu^+ \rightarrow e^+e^+e^-$ with neutrino oscillation.

Figure 1.2: Feynman diagrams of possible SM muon decays [10].

As the W^+ mass of $80.4 \text{ GeV}/c^2$ is much higher than the neutrino mass differences ($< 2 \text{ eV}$) [1], the decay $\mu^+ \rightarrow e^+e^+e^-$ is strongly suppressed with a branching ratio (BR) below 10^{-54} [11] and thus unobservable.

There are BSM theories that predict a much higher BR for this decay introducing new tree couplings (see Figure 1.3a) or loop contributions with new particles (see Figure 1.3b). Therefore, any observation of this process would be a clear hint for new physics.



(a) Tree diagram involving an unknown particle X.

(b) Penguin diagram with a SUSY loop.

Figure 1.3: Feynman diagrams of possible BMS muon decays [10].

1.2 Experimental Situation

Since 1953 experiments are performed to search for lepton flavour violation in muon decays (see Figure 1.4) [11–13]. Until today only upper limits for the branching ratios were found. The current upper limit for the $\mu^+ \rightarrow e^+e^+e^-$ decay is set by the SINDRUM experiment [14], whereas the best measurement for $\mu^+ \rightarrow e^+\gamma$ was performed by the MEG experiment [15].

SINDRUM

From 1983-86, the SINDRUM experiment was in operation at the Paul-Scherrer-Institut (PSI) in Villigen, Switzerland. Because no signal event was detected, an upper limit for the branching ratio $\text{BR}(\mu^+ \rightarrow e^+e^+e^-) < 10^{-12}$ could be set at 90% confidence level (CL) [14].

In the experiment, which was placed inside a solenoid magnetic field of 0.33 T, muons with a momentum of about 28 MeV/c were stopped in a hollow double-cone target. The decay products were measured by five tracking layers of multiwire proportional chambers and an array of scintillators for triggering and timing measurements.

MEG

To search for the LFV decay $\mu^+ \rightarrow e^+\gamma$ the MEG experiment uses a drift chamber to detect the positron and a liquid xenon calorimeter for the photon. It has been running at PSI since 2008 and is currently being upgraded to MEG II [16]. The current upper limit is $\text{BR}(\mu^+ \rightarrow e^+\gamma) < 5.7 \cdot 10^{-13}$ at 90% CL [15].

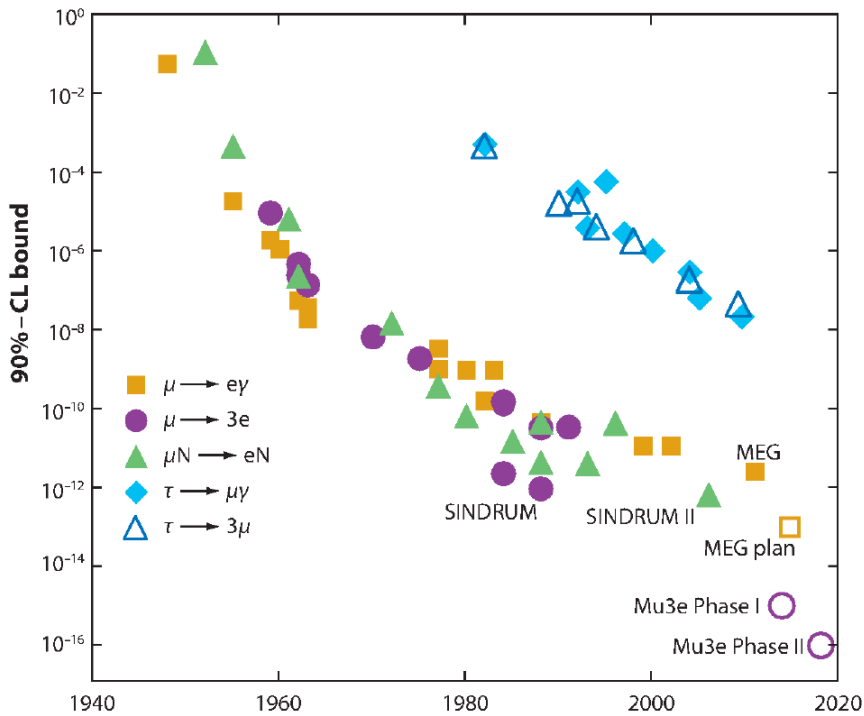


Figure 1.4: The history of LFV muon decay experiments, adapted from [11].

2 The Mu3e Experiment

2.1 The Mu3e Experiment

Mu3e is an experiment to search for the lepton flavour violating decay $\mu^+ \rightarrow e^+e^+e^-$ [17]. It is aiming to be sensitive for better than one signal decay in 10^{16} muon decays. This would increase the sensitivity by four orders of magnitude compared to the current upper limit given by SINDRUM.

To perform the experiment on a reasonable time scale, a very high muon stopping rate of $O(10^9/\text{s})$ is needed. Consequently, the main challenges for the detector design are to handle high data rates and to have a very efficient accidental background suppression.

For the latter, a very precise vertex fitting $< 200 \mu\text{m}$ as well as a momentum resolution below $0.5 \text{ MeV}/c$ and an excellent time resolution $< 100 \text{ ps}$ are needed.

The main limiting factors for the momentum and vertex resolution is multiple Coulomb scattering of the decay electrons in the detector material. Thus, the material budget of the detector must be as low as possible.

2.1.1 The Signal Decay

The muons will be stopped in a target to decay at rest. Thus the total momentum of the decay electrons is vanishing:

$$\vec{p}_{tot} = \sum_{i=1}^3 \vec{p}_i = 0. \quad (2.1)$$

The decay at rest constrains the total energy to be equal to the rest mass of the muon:

$$E_{tot} = \sum_{i=1}^3 E_i = m_\mu \cdot c^2 \approx 105.7 \text{ MeV}. \quad (2.2)$$

In summary, the signal decay is given by three electrons with a vanishing total momentum and an energy between $m_e c^2 \approx 0.5 \text{ MeV}$ and $1/2 \cdot m_\mu \approx 53 \text{ MeV}$ coming from a common vertex and being coincident in time.

2.1.2 Background Decays

Any background is due to fake signals that can be divided into two groups: internal conversion and random combinatorial background.

Internal Conversion

Internal conversion is the decay $\mu^+ \rightarrow e^+e^-e^+\nu_e\bar{\nu}_\mu$ (see Figure 2.1) which has a branching ratio of $3.4 \cdot 10^{-5}$ [1]. Here, the emitted photon immediately converts into an electron-positron pair.

Considering vertex and timing, this decay is indistinguishable from the signal decay. The only difference is a fraction of momentum and energy carried away by the neutrinos which cannot be detected. This clarifies the need for a very high momentum resolution. If both neutrinos have a vanishing momentum, this decay looks exactly as the signal decay. This is the only irreducible background.

In Figure 2.2, the branching ratio for the internal conversion as a function of the missing energy is plotted. The missing energy corresponds to the difference of $m_\mu \cdot c^2$ and the energy carried away by the electrons which is measured. To suppress this background sufficiently, an energy resolution below 1 MeV is needed.

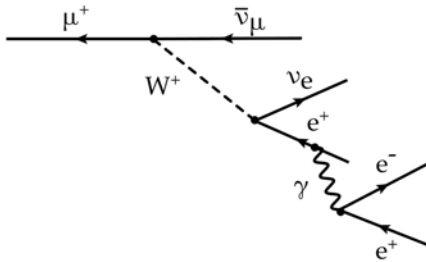


Figure 2.1: The internal conversion decay $\mu^+ \rightarrow e^+e^-e^+\nu_e\bar{\nu}_\mu$ [18].

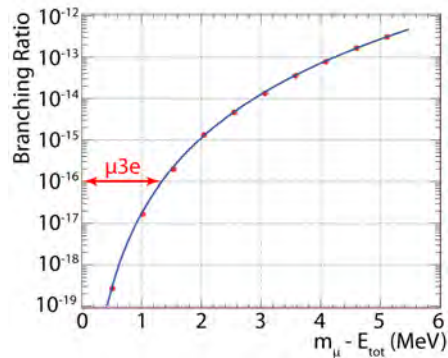


Figure 2.2: Branching ratio for the internal conversion as a function of the missing energy [19].

Random Combinatorial Background

Due to a limited spatial resolution two nearby vertices cannot be properly separated if they are too close together.

As can be seen in Figure 2.3a two positrons from the dominant Michel decay $\mu^+ \rightarrow e^+\nu_e\bar{\nu}_\mu$ (see Figure 1.2a) can be accidentally combined with an electron, for example produced by photon conversion or Bhabha scattering. Another possibility is the

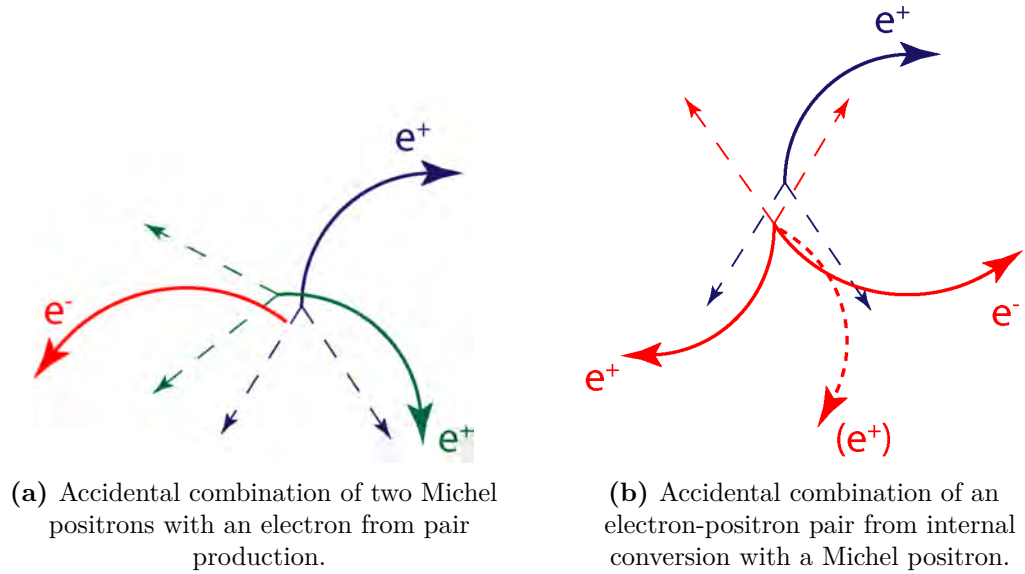


Figure 2.3: Possible combinatorial background.

combination of an electron and a positron from the internal conversion process $\mu^+ \rightarrow e^+e^-e^+\nu_e\bar{\nu}_\mu$ with a Michel positron (see Figure 2.3b).

2.1.3 Experimental Concept

As discussed above, for an efficient background suppression high rate capabilities as well as excellent spatial, time and momentum resolution are crucial.

The basic concept of the Mu3e experiment is to measure the momenta of the muon decay electrons in a solenoidal magnetic field of 1 T with a silicon pixel detector. Because multiple Coulomb scattering in the detector material is the limiting factor for the momentum resolution, minimizing the material budget below 1‰ of radiation length per layer in the active detector region is essential.

In Figure 2.4 a schematic view of the detector design is shown. The incoming muon beam will be stopped in a hollow double-cone made of aluminum to decay at rest. Four layers of very thin pixel detectors are arranged in two double layers (black) to track the decay electrons. Furthermore, scintillating fibres (grey) are used for precise timing measurements. As the experiment is placed in a magnetic field, the electrons are curled back and detected again by another double layer of pixel sensors. Finally, they are stopped in scintillating tiles which again yield precise timing information.

Pixel Detector The Mu3e pixel detector consists of High-Voltage Monolithic Active Pixel Sensors (HV-MAPS) with a pixel size of $80 \times 80 \mu\text{m}^2$. The chips are thinned down

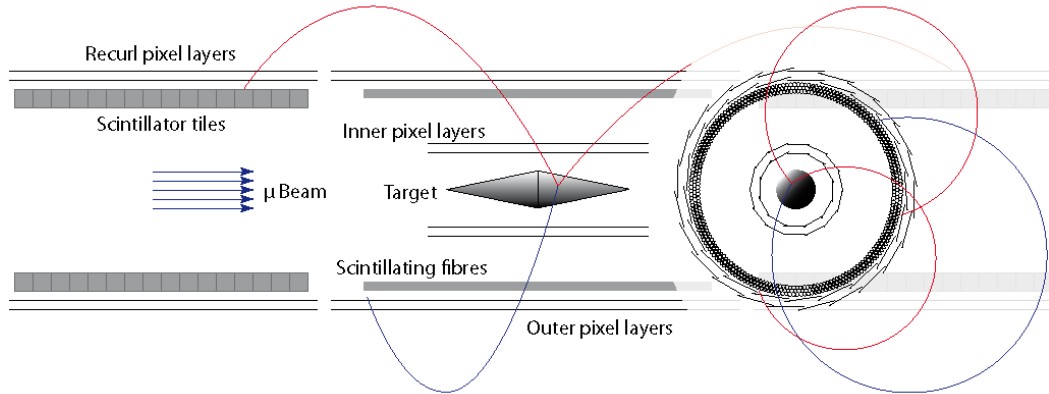


Figure 2.4: Schematic drawing of the detector design. The blue and the red lines represent recurling positrons and an electron from a signal decay. On the right side: view along the beam axis [17].

to $50 \mu\text{m}$ and have a size of $1 \times 2 \text{ cm}^2$ in the inner layers, and $2 \times 2 \text{ cm}^2$ in the outer and the recurl layers [20, 21]. With 275 million pixels an area of more than 1 m^2 will be covered.

In contrast to the classical MAPS technology, the ionization charges are collected by drift due to an applied high voltage (HV). This leads to a much faster charge collection compared to the diffusion process in MAPS. In addition, the radiation tolerance is improved. Several prototype chips are tested [22–24].

The chips will be glued on a self-supporting Kapton structure (see Figure 2.5) with a thickness of $25 \mu\text{m}$ and wire bonded to Kapton flexprint cables for power supply and readout. The triggerless readout will be done by zero-suppressed serial 800 Mbit/s Low Voltage Differential Signaling (LVDS) (see Subsection 3.1.1) [25–27].

Fibre Detector The pixel detector will be read out in 50 ns time frames. Due to the high decay rate of $2 \cdot 10^9/\text{s}$ about 100 decays per frame occur in the detector acceptance. Thus, a more precise timing measurement is needed and provided by the scintillating fibre detector.

The fibre detector consists of two or three layers of scintillating fibres with a diameter of $250 \mu\text{m}$ forming ribbons. The light produced by scintillation will be read out with arrays of silicon photo-multipliers (SiPM) mounted at both ends of the ribbons [28].



Figure 2.5: First mechanical prototype of the Kapton support structure for the inner two layers (length: 12 cm).

Tile Detector The third sub-detector is a scintillating detector consisting of $7.5 \times 7.5 \times 5 \text{ mm}^3$ tiles which are also read out by SiPMs. It will be placed right underneath the recurled pixel double-layer.

As this is the last measurement of the decay particles more material can be used. This leads to a detection efficiency close to 100% and a very high timing accuracy below 100 ps [29].

Detector Environment As mentioned above, the whole detector will be placed in a solenoidal homogeneous magnetic field of 1 T to bend the electron tracks. The front-end electronics will be placed directly on the muon beam pipe. For cooling, the whole detector volume will be filled with a circulating helium atmosphere. In addition, channels in the Kapton support structure will be flushed with gaseous helium for cooling of the pixel detectors [30–32].

2.1.4 The Readout Concept

In Figure 2.6, a schematic of the Mu3e readout chain is shown. The pixel sensors as well as the fibre and tile detectors will be connected to so-called front-end FPGAs (field programmable gate arrays, see Subsection 5.1.1). These FPGAs will be located directly on the beam pipe inside the detector.

The connection between the pixel detectors and the front-end FPGAs will be realized by serial 800 Mbit/s LVDS links (low voltage differential signalling, see Subsection 3.1.1) which will consist of tiny aluminum traces on Kapton. The manufacturing and performance tests of these so-called flexprints are the main scope of this work (see Chapter 4).

From the front-end FPGAs, the data will be sent out from the detector to FPGA-driven readout boards via high-speed optical links. Thus, a galvanic separation is guaranteed.

The data from the readout boards will then be transmitted via high-speed optical links to a GPU (graphical processing unit) filter farm where an online track and event reconstruction will be performed. Events of interest will then be sent to a data collection server which stores them in a mass storage system.

2.1.5 The Muon Beam

As an extremely high number of muons needs to be stopped to decay, a very intense muon beam is required. Therefore, the Mu3e experiment is supposed to be run at the Paul-Scherrer-Institut (PSI) in Switzerland, which operates the world's most intense muon source.

The PSI operates a cyclotron to accelerate protons which hit a carbon target, where pions are created as secondary particles. Slow pions decay immediately into muons which are collected in the $\pi E5$ beamline so that a low momentum muon beam with a rate of $2 \cdot 10^8$ 1/s is provided for a first phase of the Mu3e experiment.

In a second phase, the Mu3e experiment aims to improve the sensitivity by another order of magnitude. Therefore, a more intense muon beam is needed. Such a beam could be provided by the planned High intensity Muon Beamline (HiMB) for which the protons from the cyclotron mentioned above will be shot on the Swiss Spallation Neutron Source (SINQ) target [33]. There, a high number of muons will be created as a by-product and could be collected by the HiMB to provide a muon rate of $2 \cdot 10^9$ 1/s.

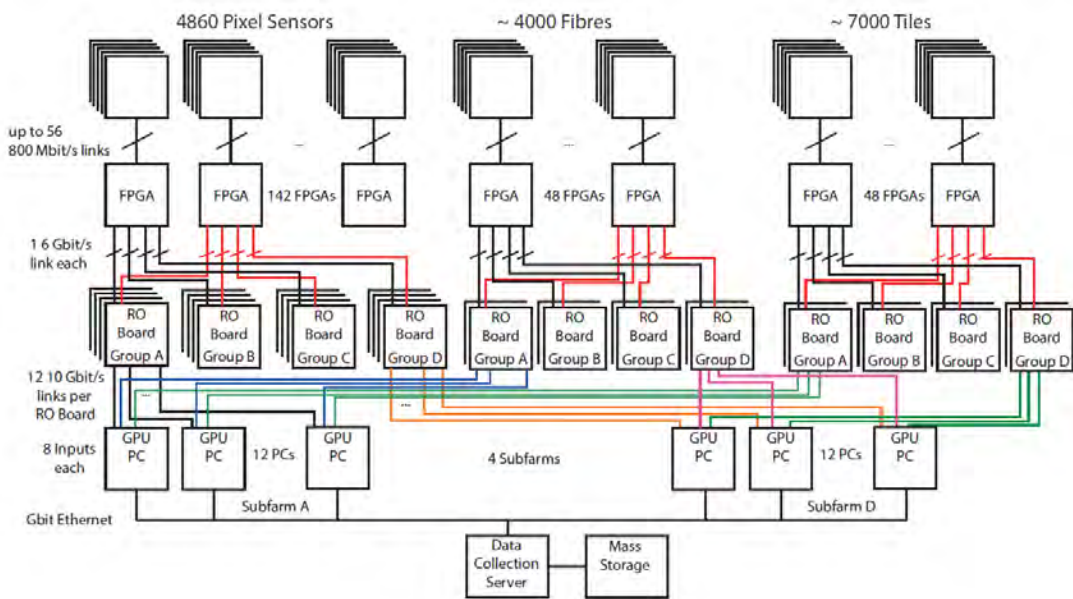


Figure 2.6: Schematic of the Mu3e readout chain consisting of three stages.

3 Basics of Data Transmission

Data transmission is the transport of information from one point to another whereby the data is represented by a physical signal [34].

3.1 Signals

A signal is the time-dependent magnitude of an observable. Electrical signals can be represented by a voltage or current. Also electromagnetic waves (optical or radio) can be used. To have an effective content of information, the time evolution of the signal must be unpredictable because otherwise the receiver can foresee incoming data which makes the transmission redundant [35].

Analogue Signals

An analogue signal is continuous in time and amplitude. In principle, every classical physical observable like brightness, temperature, or pressure can be understood as an analogue signal. Mathematically, it can be described by a smooth function of time [36].

Digital Signals

On the contrary, a digital signal consists of a sequence of discrete values. That is to say, there is only a limited set of well distinguishable values which can be attained and which are furthermore only defined at periodic points in time. An analogue signal can be transformed into a digital signal by quantisation and sampling in constant time intervals [36].

In electronics, it is common to use merely the two Boolean values 0 (false) and 1 (true) which are associated to two logic voltage levels or the transitions between those. The binary numeral system provides the theoretical basis to use binary codes (sequences of zeros and ones) for digital information processing of all kinds.

3.1.1 Low Voltage Differential Signaling

Low Voltage Differential Signaling (LVDS) is an interface standard for high-speed data transmission. It describes the physical layer which means that it only comprises

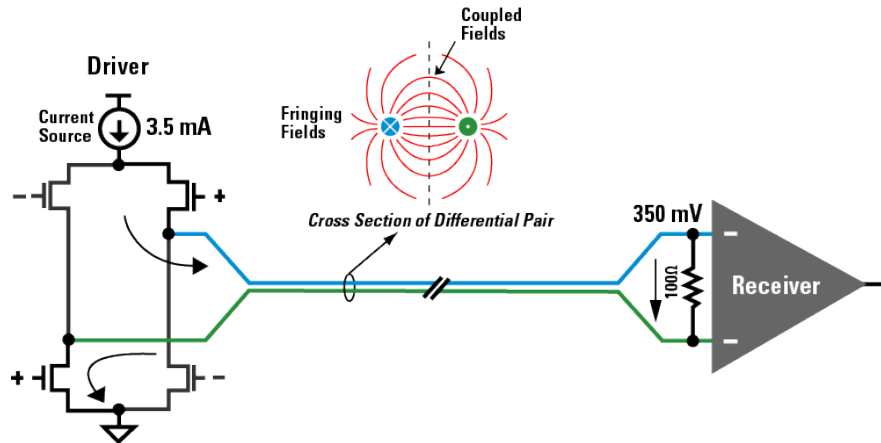


Figure 3.1: Schematic drawing of a basic LVDS circuit. Also, the field coupling of the differential pair is shown [38].

the mechanical and electronic components, i.e. the hardware, of a physical link but no encoding schemes or protocols [37].

Figure 3.1 shows the architecture of an LVDS link. A current source is injecting a constant current of 3.5 mA into the circuit. Transistors work as switches to control the direction of the current towards the receiver. At the receiver side, there is a 100 Ω terminating resistor at which a voltage of 350 mV drops according to Ohm's law.

The receiver, which is a comparator with a transition threshold of about 50 mV, senses the polarity of the signal to determine the logic state being transmitted.

LVDS has the advantage of generating very low electromagnetic noise due to the closely coupled wires. As they carry the same current in opposite directions, most of the radiation is cancelled. For the same reason, an LVDS link is relatively insensitive to external electromagnetic noise because the noise will nearly equally affect both wires and cancel out. This means that there is only very little cross-talk between adjacent wire pairs even if they are close to each other.

Another considerable advantage of LVDS is the low power consumption because of the low voltage and little radiative losses compared to other concepts of signaling. The power consumption is particularly low if it can be ensured by the transmitter side that there is no disparity, i.e. the number of ones equals the number of zeros transmitted, because in this case there is not even a net current averaged over time (see 8b/10b encoding below).

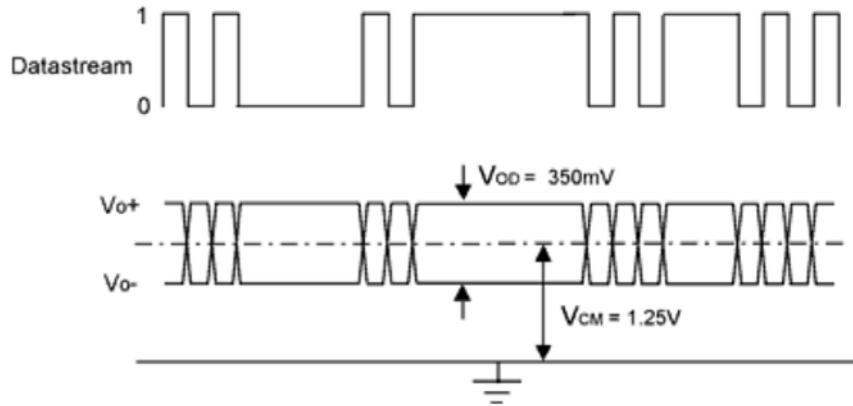


Figure 3.2: A binary datastream and the corresponding voltage dropping across the terminating resistor [39].

An LVDS connection is a serial link which means that the data is transmitted bit after bit and not in parallel (except when using several LVDS links in parallel). In Figure 3.2, an arbitrary binary datastream and the corresponding voltage levels are shown.

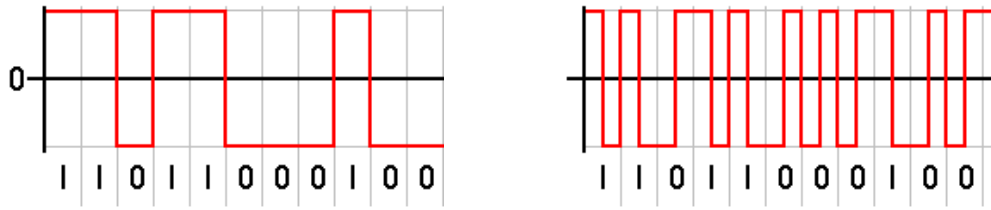
3.1.2 Data Encoding

Encoding is an injective mapping to transform data, i.e. a series of logic states, into a pattern suitable for transmission. The purpose of so-called **line codes** is to specify how the bit states '0' and '1' are represented in a signal. Because different transmission media have different properties, there are several schemes to match these characteristics.

The simplest possible code is the **non-return-to-zero code (NRZ)** (see Figure 3.3a). Ones and zeros are represented by two distinct logic levels of the signal and form a continuous sequence. Using this code can cause problems if a long sequence of subsequent ones or zeros is transmitted because in this case the logic level remains constant over a long period so that the synchronization with the underlying clock can be lost [40].

Another line code is the **Manchester code** in which falling and rising edges, i.e. the transitions between the two logic levels, represent ones and zeros, respectively. With this code clock recovery (see below) is relatively easy due to frequent transitions. A disadvantage is that twice the bandwidth compared to NRZ is required to be able to send subsequent ones or zeros (see Figure 3.3b) [42].

Line codes are not only used to specify how ones and zeros are represented in a signal. They also provide schemes how to encode bit words of a certain length in a bit pattern



(a) The non-return-to-zero code: ones and zeros are represented by two logic levels of the signal. (b) The Manchester code: ones and zeros are represented by falling and rising edges respectively.

Figure 3.3: The bit pattern "11011000100" represented in two commonly used line codes: the NRZ and the Manchester code [41].

with properties suiting the physical link [43]. Furthermore, additional information can be contained for the following purposes:

- If there is no extra clock transmission line sending "0101..." continuously, the clock has to be recovered from the data stream (**clock recovery**). Therefore a high transition rate between the logic levels is favourable.
- Some encoding schemes provide the possibility to send either data or a predefined control sequence of bits. If transmitting a continuous bit stream, **control words** can be used to identify bit packets (words). Thus, the bit stream can be cut into words of a certain length.
- For some physical layers, like LVDS, it is desirable to have **DC balance**, i.e. to send an equal number of ones and zeros to achieve a vanishing net current. By an encoding scheme like 8b/10b this can be accomplished.
- A **detection of transmission errors** is possible if bit patterns are used for which a single bitflip yields an invalid word.

8b/10b Encoding

The **disparity (dp)** of a bit pattern is given by the difference in number of ones and zeros, counting ones as $-1/2$ and zeros as $1/2$. If considering a continuous data stream, the **running disparity (rd)** is defined as the running sum over all previously transmitted words.

For 8 bit words encoded in 10 bits it is possible to ensure DC balance in a long run. That is because with 8 bits $2^8 = 256$ words can be created, whereas with 10 bits there are $2^{10} = 1024$ combinations. Regarding the restrictions that the 10 bit patterns shall

Word	Data	dp=-1	dp=+1	Word	Data	dp=-1	dp=+1
D.00	00000	100111	011000	D.16	10000	011011	100100
D.01	00001	011101	100010	D.17	10000	100011	
D.02	00010	101101	010010	D.18	01010	010011	
D.03	00011	110001		D.19	01011	110010	
D.04	00100	110101	001010	D.20	01100	001011	
D.05	00101	101001		D.21	01101	101010	
D.06	00110	011001		D.22	01110	011010	
D.07	00111	111000	000111	D.23	10111	111010	000101
D.08	01000	110001	000110	D.24	11000	110011	001100
D.09	01001	100101		D.25	11001	100110	
D.10	01010	010101		D.26	11010	010110	
D.11	01011	110100		D.27	11011	110110	001001
D.12	01100	001101		D.28	11100	001110	
D.13	01101	101100		D.29	11101	101110	010001
D.14	01110	011100		D.30	11110	011110	100001
D.15	01111	010111	101000	D.31	11111	101011	010100
K.28	11100	001111	110000				

Table 3.1: 5b/6b encoding scheme. For several 5 bit words two different patterns with disparity $dp = \pm 1$ exist. D.x mark the $2^5 = 32$ possible data words, K.28 is a control word [26].

suffice a disparity of 0 or ± 2 and never have more than five equal subsequent bits, 584 of the possible 1024 combinations are left.

One way of implementing this concept has been developed by IBM in 1983 [44]. The 8 bits of a word are split into two parts and are treated separately according to an 5b/6b and an 3b/4b part (see Tables 3.1 and 3.2), respectively. During the data transmission, the running disparity is determined to control the combination of 6 bits and 4 bits being used to satisfy the condition $dp = 0$ or $dp = \pm 1$.

Besides the advantage of DC balancing, this encoding scheme comprises some control words (so-called K-words) which do not encode data but can be used for clock recovery and phase alignment before beginning to transmit user data or to bypass phases when no actual data is transmitted to retain the synchronization. The K.28.7 word is of particular importance because it does not result from a single bit flip in the data stream.

Word	Data	dp=-1	dp=+1	K-Word	Data	dp=-1	dp=+1
D.x.0	000	1011	0100	K.x.0	000	1011	0100
D.x.1	001		1001	K.x.1	001	0110	1001
D.x.2	010		0101	K.x.2	010	1010	0101
D.x.3	011	1100	0011	K.x.3	011	1100	0011
D.x.4	100	1101	0010	K.x.4	100	1101	0010
D.x.5	101		1010	K.x.5	101	0101	1010
D.x.6	110		0110	K.x.6	110	1001	0110
D.x.P7	111	1110	0001	K.x.7	111	0111	1000
D.x.A7	111	0111	1000				

Table 3.2: 3b/4b encoding scheme. For several 2 bit words two different patterns with disparity $dp = \pm 1$ exist. For D.x.7 either P7 or A7 is used to ensure that in the resulting 10 bit pattern never more than five equal bits occur. The K.x.y words can be combined with the K.28 word of Table 3.1 to form a control word [26].

3.2 Transmission Lines

Only for direct and very low frequency alternating currents, electric wires can be characterized solely by their ohmic resistance. If the wavelength of a signal is in the order of the length of the link, this simple model is not sufficient any more.

Instead, a description as a transmission line is appropriate. This comprises not only the resistance of the wire but also its capacitance and inductance (see Figure 3.4). In place of the total resistance R , the inductivity L and the capacitance C their normalized (i.e. per length dx) counterparts R' , L' and C' are used. G' represents the conductance of the dielectric material between the transmission line and ground.

Within this model, a real wire is described as an infinite series of such elements.

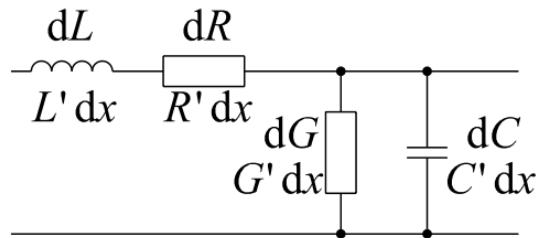


Figure 3.4: Equivalent circuit diagram of an infinitesimally short piece of a transmission line with normalized inductance L' and resistance R' coupled to ground via G' and C' [45].

3.2.1 The Characteristic Impedance

If the transmission line is homogeneous along its length, a single parameter is sufficient to describe its behaviour: the **characteristic impedance** Z_0 . It is equal to the ratio of the complex voltage and the complex current of a wave travelling along the line.

It can be shown (see [46]) that Z_0 is given by

$$Z_0 = \sqrt{\frac{R' + i\omega L'}{G' + i\omega C'}} . \quad (3.1)$$

Note that Z_0 is independent of the length of the transmission line. For an ideal conducting material ($R' = 0$) and an ideal dielectric ($G' = 0$) or high frequencies ($R' \ll i\omega L'$ and $G' \ll i\omega C'$) equation 3.1 reduces to

$$Z_0 = \sqrt{\frac{L'}{C'}} , \quad (3.2)$$

so that the characteristic impedance is also independent of the frequency. In such cases, Z_0 is not related to the ohmic resistance of a wire which causes an attenuation of the amplitude of a transmitted signal and is self-evidently dependent on the length of the transmission line. The characteristic impedance is merely a parameter to describe a wire's high-frequency behaviour.

When considering a pair of transmission lines with opposite current, which is the case for LVDS, another quantity is of importance: the **differential impedance** Z_{diff} . It is defined as the ratio of the differential voltage V_{diff} and the current I_1 on one line [47].

Due to an inductive coupling between the lines, a current I_1 in one trace will cause a current $\alpha \cdot I_1$ in the second trace with $\alpha \in (0, 1)$ being the coupling constant. A calculation, which can be found in [48], yields

$$Z_{\text{diff}} = 2Z_0(1 - \alpha) . \quad (3.3)$$

The differential impedance is of particular importance for reflections which occur if wires or other electric components with different characteristic impedances are connected. The reflection coefficient Γ is given by

$$\Gamma = \frac{Z_{\text{diff},b} - Z_{\text{diff},a}}{Z_{\text{diff},a} + Z_{\text{diff},b}} , \quad (3.4)$$

where $Z_{\text{diff},a}$ and $Z_{\text{diff},b}$ correspond to two arbitrary connected components and $Z_{\text{diff}} = R$ in case of an ohmic terminating resistor. Γ is in the range of -1 to 1 and negative values correspond to a reflection with a phase shift by π . Obviously, the characteristic

impedance of all components of an electric circuit should be matched as good as possible to ensure proper signal propagation and minimize reflections [49].

3.2.2 Microstrips

Microstrips are a certain type of transmission lines which are commonly used on printed circuit boards (PCBs) and flexprint cables (see Chapter 4). They are suited for signals in the microwave range (300 MHz to 300 GHz).

Differential Microstrips

A microstrip consists of a conducting trace which is separated from a ground (or other constant potential) plane by a dielectric layer called substrate. For LVDS links (see Subsection 3.1.1) a pair of wires is needed. When designing a PCB, the trace width w , the trace separation s , the trace thickness t , and the dielectric thickness h , as well as the dielectric constant of the substrate ϵ_r (see Figure 3.5a) need to be taken into account to match the impedance to the other electric components for minimal reflections.

Therefore, the following equation can be used for differential microstrips [50]. This approximation is valid for ratios of w/h between 0.1 and 3.0.

$$Z_{\text{diff}} = \frac{174}{\sqrt{\epsilon_r + 1.14}} \ln \left(\frac{5.98 \cdot h}{0.8 \cdot w + t} \right) (1 - 0.48 \cdot e^{-0.96 \frac{s}{h}}) \quad (3.5)$$

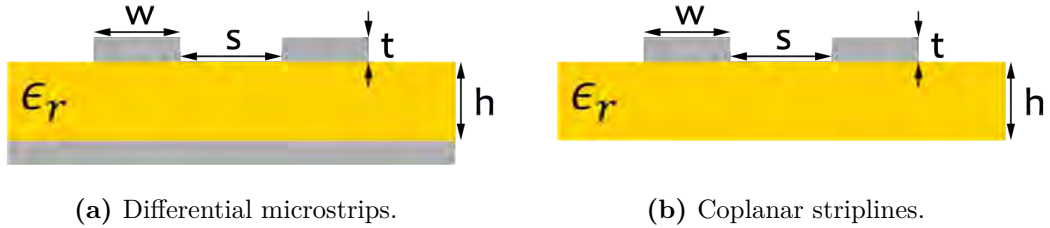


Figure 3.5: Profiles of two kinds of microstrips.

Coplanar Striplines

At first appearance, coplanar striplines seem to be very similar to differential microstrips (see Figure 3.5b), but there is a crucial difference when calculating the characteristic impedance. This is because in case of the latter, there is a clear boundary condition for the electric field surrounding the conducting traces due to the ground plane. According to [51], the impedance Z_0 of a coplanar stripline can be calculated by

$$Z_0 = \frac{120\pi}{\sqrt{\epsilon_{\text{eff}}}} \frac{K(k_0)}{K(k'_0)}, \quad (3.6)$$

where ϵ_{eff} is an effective dielectric constant given by

$$\epsilon_{\text{eff}} = 1 + (\epsilon_r - 1) \cdot \frac{1}{2} \frac{K(k')}{K(k)} \frac{K(k_0)}{K(k'_0)} \quad (3.7)$$

with $K(\bullet)$ being the elliptic integral of first kind and

$$k_0 = \frac{s/2}{s/2 + w}, \quad k'_0 = \sqrt{1 - k_0^2}, \quad (3.8)$$

$$k = \frac{\tanh \frac{\pi s}{4h}}{\tanh \pi \frac{w+s/2}{2h}}, \quad k' = \sqrt{1 - k^2}. \quad (3.9)$$

For practical purposes, $\alpha \approx 0$ and therefore $Z_{\text{diff}} \approx 2Z_0$ is assumed for coplanar striplines within the scope of this thesis.

Typically, PCBs and flexprints with (differential) microstrips are produced in lithographic processes consisting of many steps in which multiple substrate and copper layers are assembled. An overview of typical dimensions of microstrips in standard and leading edge processes is given in Table 3.3.

	copper thickness t	trace width w	trace separation s	dielectric thickness h
Multilayer PCB (standard process) [52]	$\geq 50 \mu\text{m}$	$\geq 100 \mu\text{m}$	$\geq 100 \mu\text{m}$	$\geq 60 \mu\text{m}$
Multilayer PCB (advanced process) [52]	approx. $25 - 30 \mu\text{m}$	$\geq 75 \mu\text{m}$	$\geq 75 \mu\text{m}$	$\geq 60 \mu\text{m}$
Flexprint (leading edge) [53]	$\geq 5 \mu\text{m}$	$\geq 20 \mu\text{m}$	$\geq 25 \mu\text{m}$	$\geq 25 \mu\text{m}$

Table 3.3: Typical parameters for microstrips on PCBs and flexprints.

3.3 Signal Quality Checks

Once a physical link has been realized, it needs to be tested to ascertain how reliable data can be transmitted. There are mainly two concepts which will be introduced in the following.

3.3.1 Bit Error Rate Tests (BERTs)

A **bit error rate test (BERT)** is a method to determine the quality of a transmission link for digital data transmission. The **bit error rate (BER)** is the ratio of the number of wrongly transmitted bits k and the total number of transmitted bits n and represents an estimation for the probability p for an error to occur if one bit is transmitted:

$$\text{BER} = p = \frac{\# \text{ error bits}}{\# \text{ total bits}} = \frac{k}{n} \quad (3.10)$$

In principle, a BERT can be realized by sending a deterministic datastream and comparing the incoming bits to the expected pattern at the receiver side [25]. The exact architecture of the BERT used for this thesis is described in Chapter 5.

Mathematically, a BERT can be understood as a classical counting experiment. As for every transmitted bit there are two discrete results (false or correct), it obeys a binomial distribution. For data transmission at high rates, n becomes large within seconds and the probability p for an error bit should be very small ($p \ll 1$) due to a good physical link. Therefore, the binomial distribution converges to a Poisson distribution if $\mu := \lim_{n \rightarrow \infty} p \cdot n > 0$ and the probability $P(k)$ to find k error bits in a large number of transmitted bits is given by

$$P(k) = \frac{\mu^k}{k!} \cdot e^{-\mu} . \quad (3.11)$$

For large n , the Poisson distribution converges to a normal distribution so that the standard deviation is given by $\sigma_k = \sqrt{k}$. Thus, for the BER one gets

$$\text{BER} = \frac{k}{n} \pm \frac{\sqrt{k}}{n} . \quad (3.12)$$

Upper BER Limit

If no error is detected, i.e. $k = 0$, an estimation for an upper limit of the BER must be found. In the following, a perfectly working data checker is assumed so that no error counts occur accidentally, i.e. there is no background, and no error is overlooked. According to [54] and [55], a Bayesian approach with a flat prior distribution is used. Assuming a Poisson distribution and not observing any error bits ($k_{obs} = 0$), from [55]

$$1 - \text{CL} = \sum_{k=0}^{k_{obs}} \frac{p^k \cdot e^{-p}}{k!} = e^{-p} , \quad (3.13)$$

one arrives at

$$\text{BER} \leq \frac{\log(-\text{CL})}{N} \approx \frac{2.996}{N} \text{ at } 95\% \text{ CL}, \quad (3.14)$$

where CL is the confidence level.

3.3.2 Eye Diagrams

Eye diagrams allow to visualize and determine the quality of a transmitted digital signal easily and quickly [56]. An eye diagram is constructed from a digital data-stream by superimposing the waveform of an arbitrary bit stream in a single diagram with time on the horizontal and signal amplitude on the vertical axis. Therefore, it represents the average statistics of the signal.

An ideal waveform of the digital signal would result in a square-shaped eye diagram as can be seen in Figure 3.6a. Due to impairments of the signal like attenuation, crosstalk or noise and a limited bandwidth of the transmitter, real physical signals differ from this and rather resemble the eye diagram shown in Figure 3.6b. Here, the **unit interval UI** is defined as the time it takes to transmit one bit and corresponds to the inverse of the transmission rate.

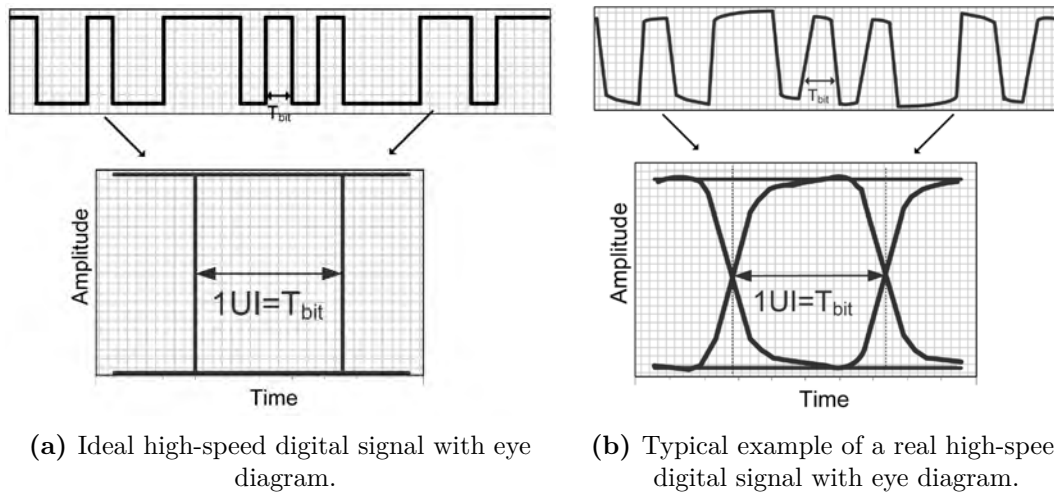


Figure 3.6: An ideal and a real arbitrary digital datastream superimposed in eye diagrams [56].

From an eye diagram a number of key parameters can be determined. These are shown in Figure 3.7 and described in detail below.

- The **zero-level** and the **one-level** are the mean values of the lower and upper logic levels, respectively. In NRZ coding they correspond to a '0' and a '1'.

- The **eye amplitude** is the difference between the two logic levels. This quantity is used by the receiver to determine whether a '0' or a '1' has been transmitted.
- The **eye height** describes the vertical opening of an eye diagram. Ideally, it would be equal to the amplitude but in reality, it is smaller due to noise or saturation effects.
- The level at which rising and falling edges cross is called **eye crossing percentage** and should be at 50% of the amplitude.
- The **eye width** corresponds to the vertical opening of an eye diagram and should ideally be equal to the unit interval.
- **Jitter** refers to variations in the transmission frequency so that rising and falling edges are slightly shifted and occur too early or too late.

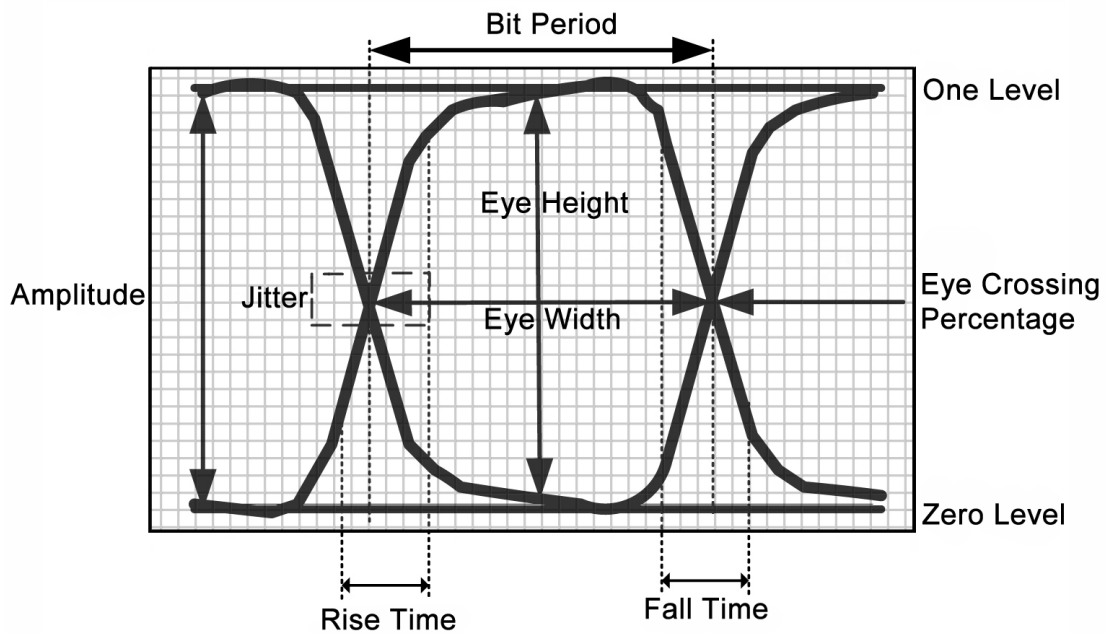


Figure 3.7: A typical eye diagram with key parameters [56] (modified).

Part II

Measurements & Results

4 Manufacturing of Kapton Flexprints

A flexprint is a bendable plastic film carrying conducting traces which consist of copper or aluminum. To manufacture flexprints, usually lithographic processes are used which resemble those for PCB production. For this thesis, it was examined in what way Kapton foils laminated with aluminum can be processed with a laser such that the aluminum evaporates in some areas whereas the Kapton is damaged as little as possible and conducting traces remain.

4.1 The Laser Platform

For manufacturing the flexprints, a PLS6MW Multi-Wavelength Laser Platform from Universal Laser Systems (see Figure 4.1) has been used. It provides a plane work area of approximately $80 \times 46 \text{ cm}^2$ on which a broad spectrum of materials can be processed with different wavelengths as the laser source can be changed. For this thesis, a CO_2 laser with a wavelength of $9.3 \mu\text{m}$ and a fibre laser with a wavelength of $1.06 \mu\text{m}$ are available.



Figure 4.1: A photo of the PLS6MW Laser Platform, taken from [57].

For processing, a material is placed on the work area and scanned with the pulsed laser. For ideal results, several parameters can be adjusted, such as laser power, laser movement velocity, pulse frequency, waveform, and vertical focus position. The laser can either treat areas (called 'rastering') by moving back and forth in x-direction while scanning the y-direction incrementally, or move along lines (called 'vectoring'). When

'rastering', the additional parameters contrast, definition and density are adjustable.

In order to blow away evaporated material and prevent the lens from being contaminated with debris, a nozzle points an air stream onto the focus of the laser. Apart from compressed air, every other gas can be used if not flammable. As light materials, such as Kapton foils, can ripple or might even be blown away by the air stream, they should be adhered to a sticky rubber mat.

Layouts must be designed as vector graphics with a third-party graphic software, such as CorelDRAW[®], and different laser settings can be assigned to the RGB-encoded colors black, red, green, yellow, blue, magenta, cyan, and orange. The laser platform is then addressed by the Windows Print System like an arbitrary printer [58].

4.2 Kapton

Kapton[®] is a multi-purpose polyimide film developed by DuPont[™]. It has an excellent balance of electrical, thermal, mechanical, physical, and chemical properties and was used in applications with a wide temperature range from -269°C up to 400°C [59]. Furthermore, it can be laminated with a thin metal layer or glued to another film of Kapton. For the Mu3e experiment $25\ \mu\text{m}$ Kapton Type HN is planned to be used for flexprints and the mechanical support structure to minimize the material budget inside the active detector region.

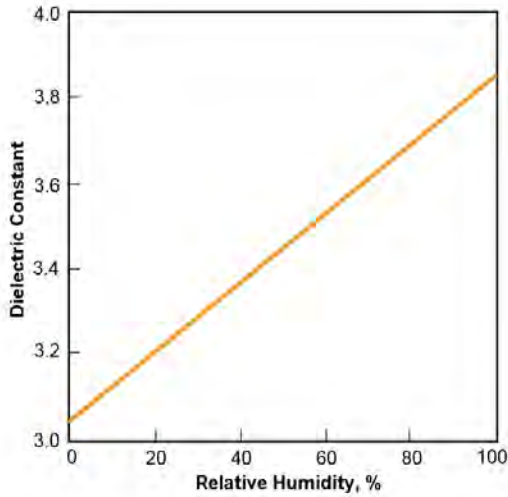
4.2.1 Physical Properties

Kapton is mechanically stable though flexible and retains its physical properties over a wide temperature range. It does not melt or burn and has the highest UL-94 flammability rating: V-0 [60].

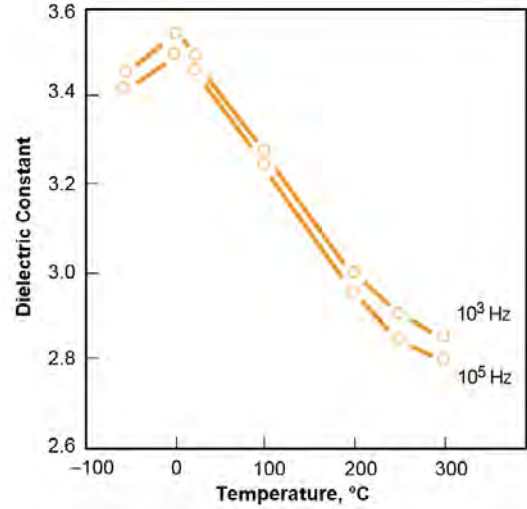
Between 360°C and 410°C a second order phase transition occurs which is assumed to be a glass transition. According to the manufacturer, different measurement techniques result in different transition temperatures [60].

4.2.2 Electrical Properties

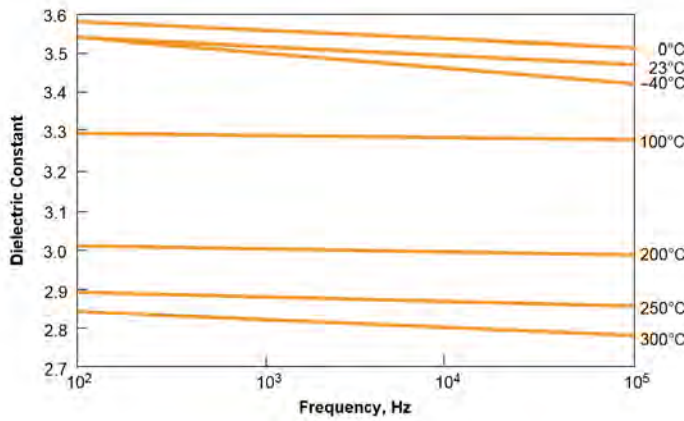
The dielectric constant ϵ_r of Kapton depends on the relative humidity of the air as well as on the temperature and the frequency. In Figure 4.2, ϵ_r is plotted versus these quantities. Assuming normal conditions and a relative humidity around 50%, ϵ_r is approximately 3.4.



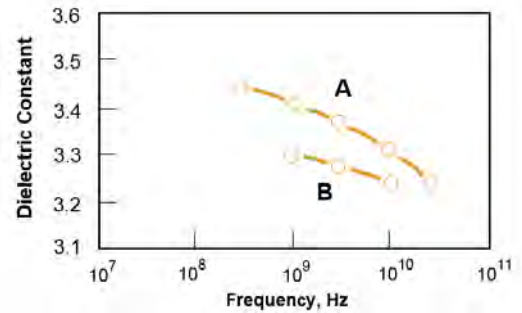
(a) ϵ_r vs. rel. humidity at room temperature, type HN film, 25 μm .



(b) ϵ_r vs. temperature for two frequencies, type HN, 25 μm .



(c) ϵ_r vs. frequency at various temperatures, type HN, 25 μm .



(d) ϵ_r vs. frequency at 25°C and 45% rel. humidity, type HN, 125 μm . B corresponds to the same measurement as A after conditioning the film at 100°C for 48 h.

Figure 4.2: Dependence of the dielectric constant ϵ_r on various quantities, from [60] (modified).

4.3 Aluminum

Though aluminum has only 63% of the electrical conductivity of copper and a lower heat conductivity [61], it is widely used in electronic applications due to its low mass density and easy processing [62, 63].

It also has a much lower atomic number Z than copper which makes it particularly interesting for the Mu3e experiment because of the multiple scattering dominated electron interactions with matter. According to [64], multiple scattering can be quantified by Θ_{MS} being the root mean square (RMS) of the central 98% of the planar scattering contribution. It is given by

$$\Theta_{MS} \propto \sqrt{\frac{x}{X_0}} \left(1 + 0.038 \cdot \log \frac{x}{X_0}\right), \quad (4.1)$$

where x is the material thickness d multiplied with its mass density ρ ($x = \rho d$), and X_0 the radiation length which can be approximated by [64]

$$X_0 = \frac{716.4 \text{ g} \cdot \text{cm}^{-2} \cdot A}{Z(Z+1) \log(287/\sqrt{Z})}, \quad (4.2)$$

where A is the mass number of the nucleus. The radiation length characterizes a material with regard to the energy loss of electromagnetically interacting particles. With the values from Table 4.1, the ratio of Θ_{MS} for aluminum and copper comes out to be

$$\frac{\Theta_{MS,\text{Al}}(d = 12 \text{ } \mu\text{m})}{\Theta_{MS,\text{Cu}}(d = 5 \text{ } \mu\text{m})} \approx 0.59. \quad (4.3)$$

Consequently, an aluminum thickness of 12 μm leads to a clearly decreased amount of multiple scattering compared to commercial leading edge flexprints (e.g. offered by Dyconex) which provide a minimal copper thickness of 5 μm (see Table 3.3).

Even repeating the calculation with a double layer of aluminum gives

$$\frac{\Theta_{MS,\text{Al}}(d = 24 \text{ } \mu\text{m})}{\Theta_{MS,\text{Cu}}(d = 5 \text{ } \mu\text{m})} \approx 0.87. \quad (4.4)$$

	thickness d	mass density ρ	atomic number Z	mass number A	rad. length X_0
Al	12 μm	2.699 $\text{g} \cdot \text{cm}^{-3}$	13	26.98	24.01 $\text{g} \cdot \text{cm}^{-2}$
Cu	5 μm	8.960 $\text{g} \cdot \text{cm}^{-3}$	29	63.55	12.86 $\text{g} \cdot \text{cm}^{-2}$

Table 4.1: Some physical properties of aluminum and copper [1].

To evaporate aluminum with a laser, it needs to be heated above its boiling point at 2519°C [63]. According to [65], the reflectivity at a wavelength of about 1 μm is in the range of 0.93 and at 10 μm it is approximately 0.98. Therefore, the fibre laser with a wavelength of 1.06 μm is used to deposit the maximal possible amount of energy in the aluminum.

4.4 Structure Sizes

4.4.1 Impedance Calculations

In a first step, the structure sizes are calculated which are needed to match $Z_{\text{diff}} = 100 \Omega$ for minimal reflections. In the tables below, several calculations are presented based on the formulas introduced in 3.2.2. A dielectric constant $\epsilon_r = 3.4$ and an aluminum thickness of 12 μm have been assumed.

trace width w [μm]	trace separation s [μm]	Z_{diff} [Ω]
10	10	328
50	50	376
100	150	468
150	150	428

Table 4.2: Calculation of the impedance for **coplanar striplines on 25 μm Kapton**. Coupling constant $\alpha \approx 0$ assumed.

trace width w [μm]	trace separation s [μm]	Z_{diff} [Ω]
35	60	100
80	100	53
100	150	38
150	150	no value*

Table 4.3: Calculation of the impedance for **differential microstrips on 25 μm Kapton**. *Equation 3.5 not valid.

trace width w [μm]	trace separation s [μm]	Z_{diff} [Ω]
80	100	101
100	150	91
150	150	63

Table 4.4: Calculation of the impedance for **differential microstrips on 50 μm Kapton**.

The comparison shows that much larger structure sizes suffice to achieve a differential impedance in the range of 100Ω with differential microstrips on $50 \mu\text{m}$ Kapton than with thinner Kapton. For the coplanar striplines, it is not possible to find structure sizes yielding a Z_{diff} close to 100Ω .

4.4.2 Test Structures

The second step was to examine down to which scales the laser platform works properly and to find optimal settings. Therefore, a series of test structures has been produced (see Figure 4.3).

All of the test structures and flexprints have been produced with the settings listed in Table 4.5. The Kapton foil was placed on a sticky rubber mat with the aluminum layer on top. In addition, the vertical position (not in the table) had to be adjusted to the thickness of the rubber mat and the Kapton. Since the calibration was not very stable and changed from day to day, it was easier to produce a quick test structure and try out different settings for the vertical position than recalibrating the laser system again.

	power [%]	speed [%]	freq. [MHz]	waveform	contrast [%]	def. [%]	density [%]
rastering	100	65	30	0	20	10	80
vectoring	100	14	30	0	20	10	80

Table 4.5: Laser settings used to produce test patterns and flexprints.

Besides the power, the speed, and the frequency of the pulsed laser, it is possible to set a value of 0 to 5 for the waveform. In [58], the different waveforms are not specified but only 0 yields proper results. A high contrast increases the laser power at edges in areas with a high density of graphical details. Definition, on the contrary, increases the laser power in areas with a low density of graphical details. A high setting for density decreases the laser power at all edges to compensate for laser lag in turning off at high speeds.

Table 4.6 summarizes the minimal structure sizes which could be produced such that the traces were still conductive and properly separated, respectively. Nevertheless, it was found out that a trace width of $80 \mu\text{m}$ does not conduct reliably at a length of $\geq 10 \text{ cm}$ (see Subsection 4.5.3).

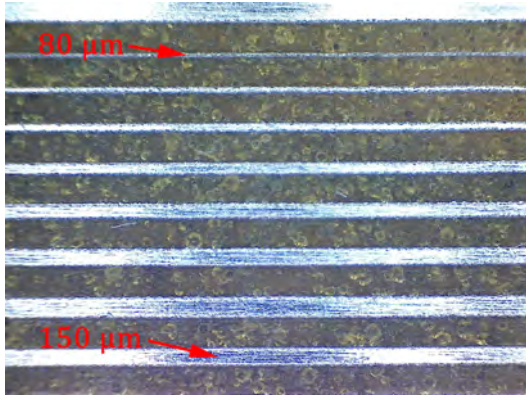
Microscopic images of the test structures are shown in Figure 4.3. One observes that the $80\text{-}100 \mu\text{m}$ separations in Figures 4.3b, 4.3d, and 4.3f have the same widths. Still,

	min. trace width [μm]	min. trace separation [μm]
horizontal	80	100 (vect.), 110 (rast.)
45°	100	100 (vect.), 140 (rast.)
vertical	100	100 (vect.), 140 (rast.)

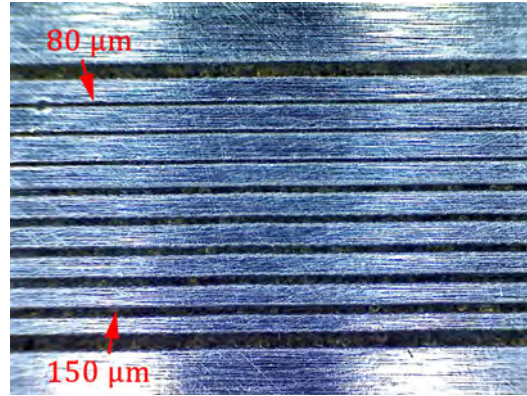
Table 4.6: Laser settings used to produce test patterns and flexprints.

these separations are not always proper. The laser would have to be run at a lower velocity for these cuts. The reason why this can still not be used for the manufacturing of flexprints is discussed in Section 4.5.1.

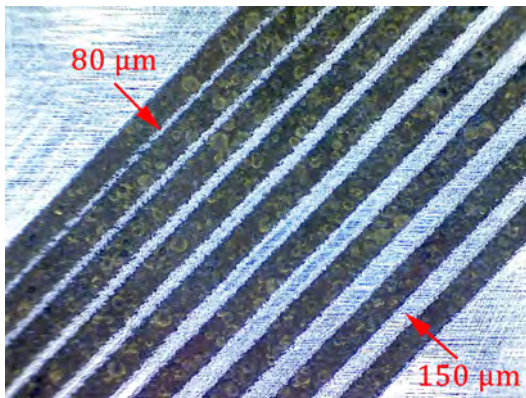
With this laser platform, it is in principle not possible to go below a trace separation of 100 μm because this is the width of a single laser cut, i.e. the radius of the laser focus. For all lines $\leq 100 \mu\text{m}$ in a layout, the laser mode is automatically changed to from 'rastering' to 'vectoring'. Therefore, the 80-100 μm cuts in Figures 4.3d and 4.3f show a better result than the 110-130 μm separations.



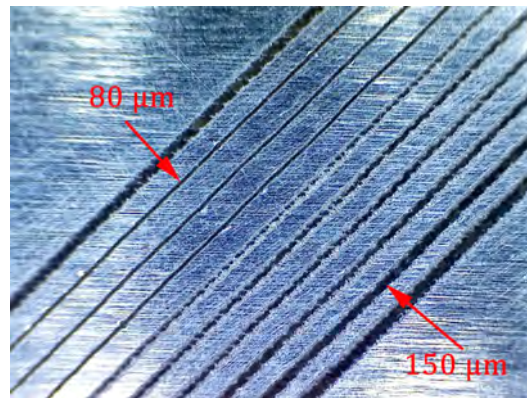
(a) Horizontal connection.



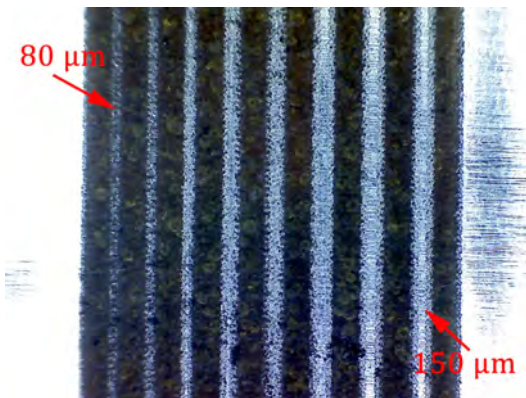
(b) Horizontal separation.



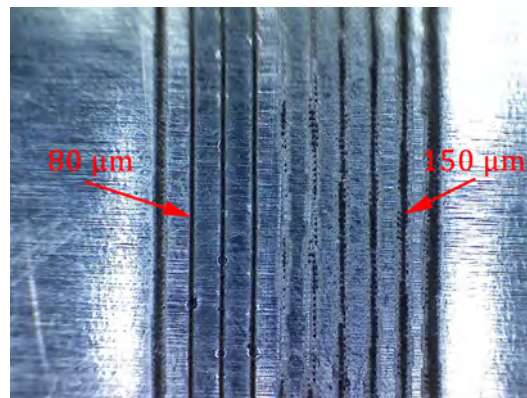
(c) 45° connection.



(d) 45° separation.



(e) Vertical connection.

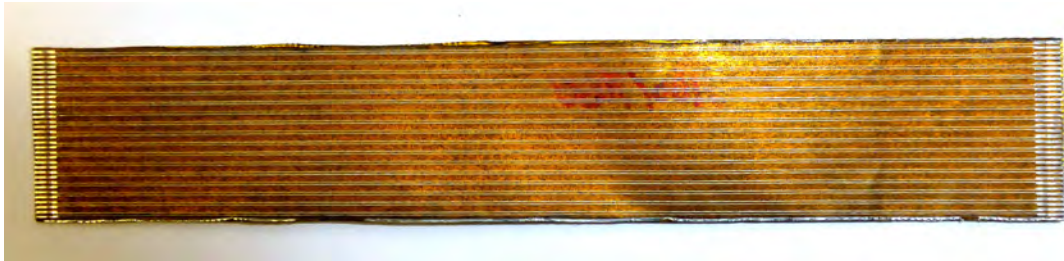


(f) Vertical separation.

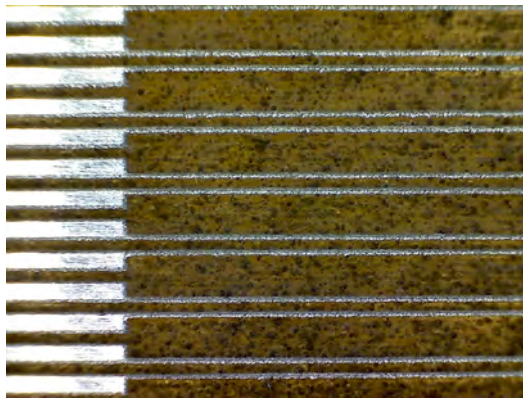
Figure 4.3: Test patterns to examine which minimal structure sizes can be achieved by rastering. All trace widths and trace separations are from $80\ \mu\text{m}$ to $150\ \mu\text{m}$ in steps of $10\ \mu\text{m}$ from top to bottom or left to right, respectively. For the connection structures, the gap is kept constant, whereas the pitch is kept constant for the separation structures.

4.5 Flexprint Cables

Multiple flexprint cables with different characteristics have been produced, examples of which are shown in Figures 4.4, 4.5, and 4.6. Various types of flexprints have been successfully produced at lengths of 10, 20, and 30 cm though broken traces were not uncommon for a trace width of $100\ \mu\text{m}$ (see Subsection 4.5.3). Flexprints with a trace width of $100\text{-}150\ \mu\text{m}$ have also been produced up to a length of 50 cm.



(a) Photo of the full flexprint.



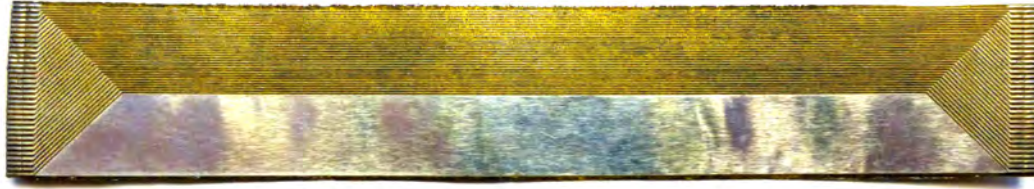
(b) Microscopic image of the traces and contact pads.

Figure 4.4: Flexprint with a trace width of $100\ \mu\text{m}$, a trace separation of $150\ \mu\text{m}$ for pairs and $650\ \mu\text{m}$ between pairs, and a Kapton thickness of $50\ \mu\text{m}$ plus aluminum ground plane. Length of the flexprint: 10 cm.

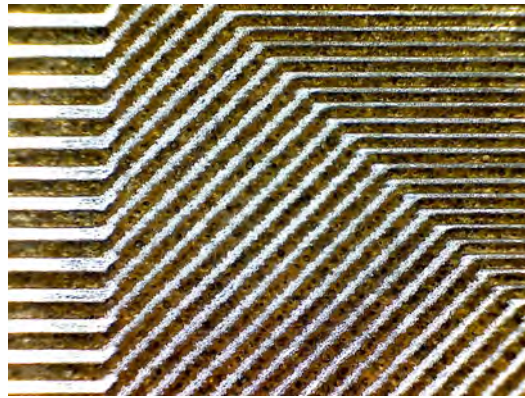
The flexprint shown in Figure 4.4 consists of 17 equal trace pairs with a large separation between adjacent trace pairs. It has only horizontal structures so that it can be produced at a higher laser velocity. This type of flexprint has also been produced with a trace width from $100\text{-}150\ \mu\text{m}$ and trace separations between $110\text{-}150\ \mu\text{m}$.

In Figure 4.5 one can see a flexprint on which all traces have the same separation of $150\ \mu\text{m}$. To meet the $0.5\ \text{mm}$ pitch of the Flexible Printed Circuit (FPC) connec-

tor, which was used to clamp the flexprints, it was necessary to introduce 45° sections. Therefore, this type of flexprint had to be manufactured with a laser velocity of 65%.



(a) Photo of the full flexprint.



(b) Microscopic image of the transition between main section, the 45° section and the contact pads.

Figure 4.5: Flexprint with a trace width of 100 μm , a trace separation of 150 μm between all traces in the horizontal section and trace width and separation of 175 μm each in the 45° section, plus aluminum ground plane. Length of the flexprint: 10 cm.

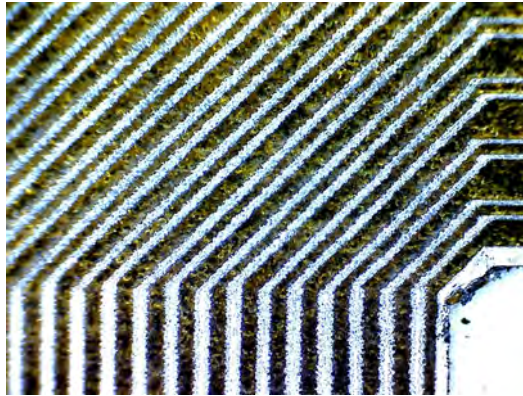
A third type of flexprints has been produced to examine the feasibility of designing flexprint cables with an FPC connector rotated by 90°. Such a flexprint can be seen in Figure 4.6. Also this flexprint type had to be manufactured with a laser velocity of 65%. This arrangement of the FPC connector is of particular interest for the assembly Mu3e experiment because of the spatial constraints.

4.5.1 Limitations

Since the laser focus has a radius of approximately 100 μm , it was expected that the minimal trace separation which can be achieved corresponds to this value. As described in Section 4.4.2, the laser mode changes to 'vectoring' for all lines $\leq 100 \mu\text{m}$ in a layout.



(a) Photo of the full flexprint.



(b) Microscopic image of the transition between main section and 45° section and the contact pads.

Figure 4.6: Flexprint with a trace width of $100\ \mu\text{m}$, a trace separation of $150\ \mu\text{m}$ between all traces in the horizontal section and trace width of $140\ \mu\text{m}$ and a trace separation of $150\ \mu\text{m}$ in the 45° section. Length of the flexprint: 10 cm.

When using the laser, it always rasters first before it vectors. Therefore, the idea was to produce flexprints first with one thick trace instead of a pair and then to cut these with a single laser movement.

However, it was observed that the mechanical laser positioning system is not precise enough to separate the thick trace exactly in the middle (see Figure 4.7). Due to this imprecision, one rather obtains two highly asymmetric traces or the laser even cuts so close to the edge that it simply reduces the width of the single trace.

For the same reason, it is not possible to process the Kapton foils with multiple laser settings successively. Trying to correct the offset in the layout itself does not solve this problem because overlapping colours (encoding different laser settings) are not converted correctly.

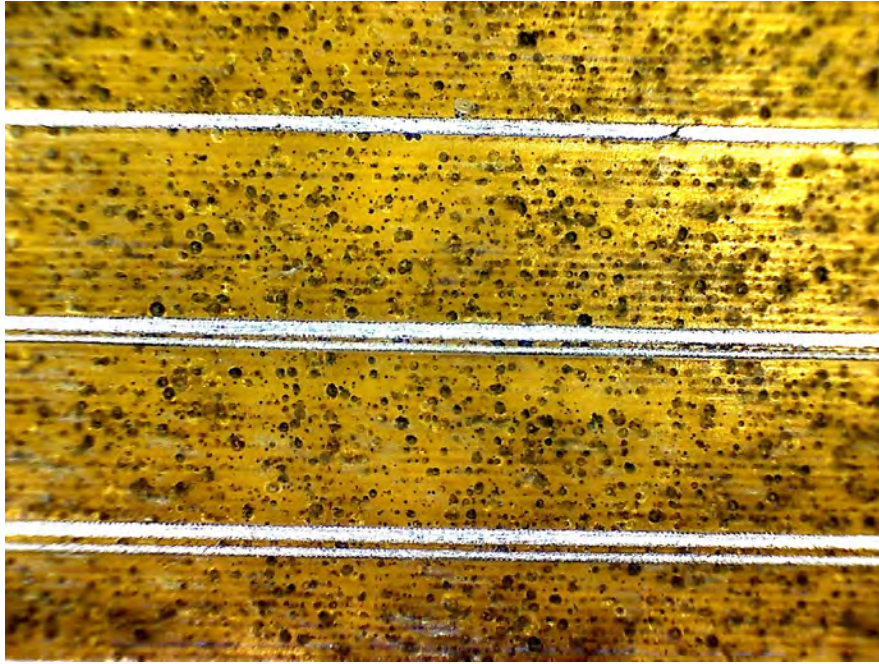


Figure 4.7: Attempt to cut a single trace into two thin traces.

4.5.2 Obtaining Different Types of Microstrips

The aluminum traces on the processed Kapton strips correspond to coplanar striplines as they are mounted on a dielectric without a ground plane.

To obtain differential microstrips, an extra aluminum layer had to be added. For this purpose, another strip of aluminum/Kapton foil of the same size has been glued onto the back side of the flexprint. Gluing the aluminum layer directly to the back side yields a dielectric thickness of $25 \mu\text{m}$ whereas gluing Kapton on Kapton yields $50 \mu\text{m}$.

For gluing, a two-component adhesive was used which is also used to build the Kapton support structure for the pixel tracker. After the adhesive was dripped onto the Kapton with the help of a syringe, the two strips were pressed together for 20-24 hours for curing. Thus, a very homogeneous distribution of the adhesive was obtained.

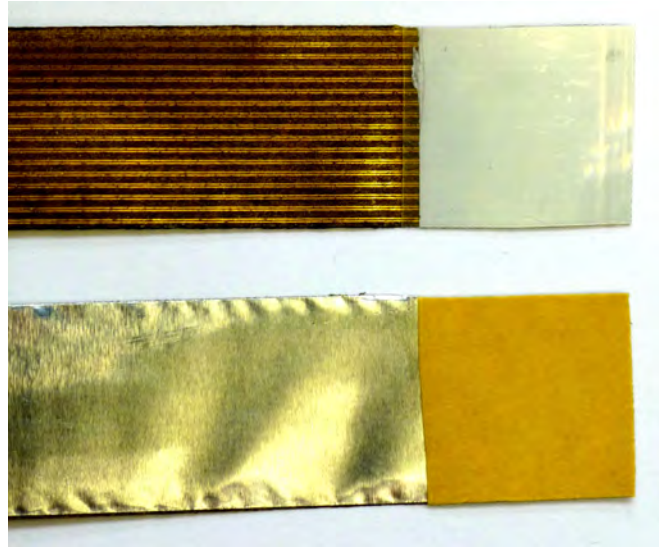


Figure 4.8: Photo showing the thickened ends of two flexprints. **Top:** adhesive tape plus plastic foil. **Bottom:** adhesive tape with one protection foil left.

4.5.3 Mechanical Properties

Connectivity and Interfaces

To achieve a proper connectivity of the flexprints to the FPC connector, they have to be pushed in and adjusted carefully since the contact pins have a width of only $200\ \mu\text{m}$. This works best with the help of a microscope.

Especially newly produced flexprints often had small aluminum filaments at their ends which occasionally shorted two traces or contacts and thus prevented proper signal propagation. These filaments could be easily removed by hand or with compressed air.

The FPC connectors require a flexprint thickness of $300\ \mu\text{m}$ which is much more than that of produced the flexprints ($37\ \mu\text{m}$ for coplanar striplines, $74\ \mu\text{m}$ for differential microstrips). For this reason and for mechanical stability, i.e. to be able to push the flexprints into the FPC connector without bending them, it is necessary to thicken their ends.

For this purpose, double-sided adhesive tape was used. As shown in Figure 4.8, it was glued onto the back side of the flexprint with one protective foil left (differential microstrips) or a small piece of a slightly thicker plastic foil (coplanar striplines). Thus, a thickness of approximately $350\text{-}400\ \mu\text{m}$ was obtained which even exceeds the required $300\ \mu\text{m}$ and worked well.

In case of the coplanar striplines, this procedure leads to an increased thickness of the dielectric at the ends of the flexprint. The dielectric constant of neither the adhesive

tape nor the plastic foil are known but a generic calculation with an assumed dielectric thickness (of pure Kapton) of $350\ \mu\text{m}$ yields $Z_0 = 174\ \Omega$ instead of $234\ \Omega$.

In case of the differential microstrips, the adhesive tape does not affect the dielectric properties of the flexprint since it is placed below the shielding aluminum plane.

Fragility

It has been observed that traces break very easily if the flexprints are unintentionally folded while pushing them into the FPC connector. Consequently, they need to be handled carefully and the adhesive tape is absolutely necessary for mechanical stability. However, bending the flexprint in a loop like in Figure 5.1 does not cause any damage.

On many of the cables a few traces were not conducting. This problem increased with growing length. For 10 cm cables broken traces occurred only rarely whereas at a length of 30 cm typically 2-3 of 17 channels did not work due to broken traces. An attempt to produce a 50 cm cable with a trace width of $100\ \mu\text{m}$ yielded only 2 working channels.

It is likely that this problem comes up because the laser platform does not work homogeneously throughout the whole table. This might be due to an imperfect calibration of the work area so that it is slightly slanted and the laser focus passes through different vertical positions.

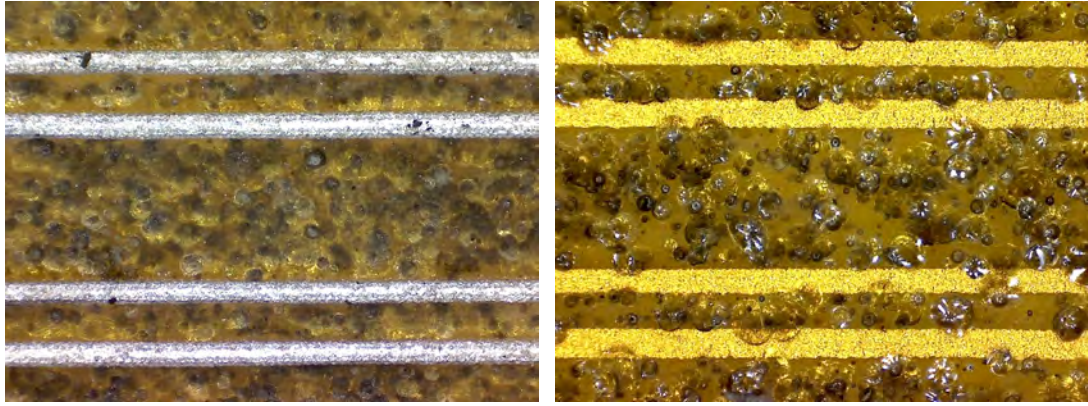
Flexprint with a trace width of $\geq 120\ \mu\text{m}$ have been successfully produced at a length of 50 cm with all channels working. From this, one concludes that a trace width of $\geq 120\ \mu\text{m}$ can be manufactured with a much higher reliability.

4.5.4 Blackening of the Kapton

The Kapton becomes darker the slower the laser is moved. The question arises what happens to the Kapton during this process and whether the dielectric properties are changed.

The image taken from the back side of the Kapton strips shows that bubbles have formed inside the Kapton and buckled the surface.

This behaviour can be understood. According to [66], Kapton changes its colour from dark brown to black if heated above a temperature of 500°C . Additionally, the gases CO and CO₂ emerge at the decomposition of the polyimide film. Since aluminum evaporates at 2519°C , the Kapton is certainly heated above 500°C for a short time. Considering also the manufacturer information that a second order phase transition is



(a) (Processed) front side.

(b) Back side.

Figure 4.9: Microscopic images of flexprints showing the blackening of the processed Kapton.

assumed to occur between 360°C and 410°C [60], it is likely that mainly two things happen:

- CO and CO₂ emerge inside the Kapton which starts decomposing due to the high temperature.
- The Kapton becomes expansible and soft as the thermal energy of the polyimide molecules exceed the binding energy of the hydrogen bonds.

As a consequence, the gas bubbles can easily expand inside the Kapton and lead to buckles at the surface which are stronger on the back side of the flexprint as the air stream of the laser platform could push them down on the front side.

The front side of the Kapton, which has been processed by the laser and carries the aluminum traces, is observed to be darker than the back side. One possibility is that this is due to burned residues of the glue between the Kapton and the aluminum foil. An additional effect could be that the aluminum might not completely be evaporated by the laser but red-hot particles fly away and possibly burn holes into the front side of the Kapton.

To find out whether this effect is enhanced by blowing the compressed air at the red-hot particles and thus supplying oxygen, the compressed air was exchanged by Argon. No observable difference has been noticed. Consequently, the oxygen does not seem to be the reason for the blackening of the Kapton.

Change of the Dielectric Properties

The influence of the blackening on the dielectric properties of the Kapton is hard to estimate. One possible assumption is that due to the gas bubbles, which have originated inside the Kapton, the dielectric constant becomes inhomogeneous and is somewhat decreased in average. To get an impression of the order of magnitude, a decline of 20% is assumed (which is certainly overestimated). Then Equation 3.5 yields a differential impedance of 98 Ω instead of 91 Ω in case of differential microstrips with a trace thickness of 100 μm and a trace separation of 150 μm on 50 μm Kapton.

Two important things can be observed:

- Z_{diff} is only weakly dependent on ϵ_r , i.e. a change of -20% of ϵ_r implies a change of only 8% of Z_{diff} .
- From $Z_{\text{diff}} \propto 1/\sqrt{1.14 + \epsilon_r}$, it can be concluded that the differential impedance grows with a declining dielectric constant.

Consequently, the influence of the partial decomposition is likely to have only a small impact on the differential impedance.

5 Performance of BERTs

In order to perform BERTs, an appropriate test setup has been developed, which is shown in Figure 5.1. The concept was to implement a data generator in an FPGA to output a continuous LVDS bitstream. The signals were conducted via the flexprints and fed back to the FPGA where they were checked for bit errors.

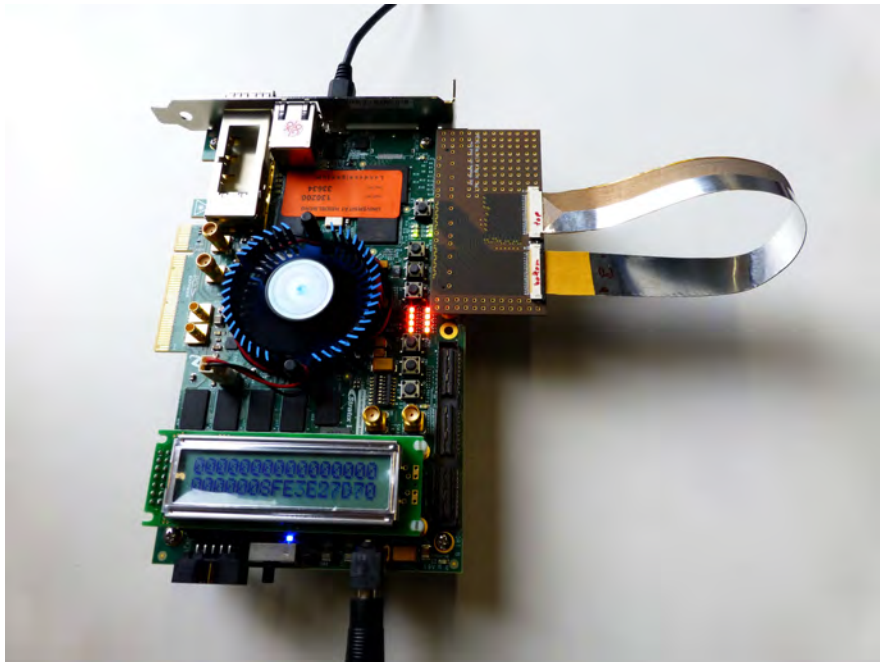


Figure 5.1: Picture showing the setup used for the BERTs comprising the FPGA development board, the HSMC adapter board and the self-manufactured flexprint.

The hardware components needed are described in detail below, followed by a presentation of the necessary software packages. After that, the explicit architecture of the firmware, which implements the BERT, is presented followed by a discussion of the results.

5.1 Hardware

5.1.1 Field Programmable Gate Array

A **field programmable gate array (FPGA)** is an integrated circuit (IC) in which a logic design can be implemented. For this purpose, it consists of multiple electronic components, such as logic array blocks, adaptive logic modules, and embedded memory blocks, which can be arbitrarily interconnected [67, 68]. The interconnections are realized by electrical switches, i.e. transistors, in the FPGA so that the device needs to be reprogrammed after every power-off.

In comparison to application specific integrated circuits (ASICs), FPGAs have a lower logic density, a higher power consumption and lower clock frequencies. But once ASICs are produced, their logic cannot be changed anymore, whereas FPGAs can easily be reconfigured. This advantage compensates the above named drawbacks for many applications [68].

For this thesis, a **Stratix V** by Altera has been used. This FPGA is optimized for high-bandwidth applications [69] and is planned to be employed on the readout boards in the Mu3e detector (see Subsection 2.1.4).

5.1.2 FPGA Development Board

The Stratix V is mounted on a PCB which provides a hardware platform for the development and prototyping of high-performance designs (see Figure 5.2). Besides supplying power for the FPGA, it provides a variety of communication ports for several interface standards. In addition, it bears three push buttons and eight DIP switches which the user can integrate in his design to communicate with the Stratix. Moreover, output data from the FPGA can be sent to 16 LEDs and an LCD display [70].

5.1.3 HSMC Flexprint Adapter Board

The Altera High Speed Mezzanine Card (HSMC) standard specifies a high-performance interface for the connection of secondary PCBs (named mezzanine cards) to the host board of an FPGA and allows for fast differential signaling on multiple parallel channels [72].

In order to create an interface between the FPGA Development Board and the flexprint cable, an adapter board had to be designed as part of this thesis (see Figure 5.3). On the bottom side, it hosts an HSMC connector to be plugged into the HSMC port of the development board, and on top two FPC connectors are mounted for the connection

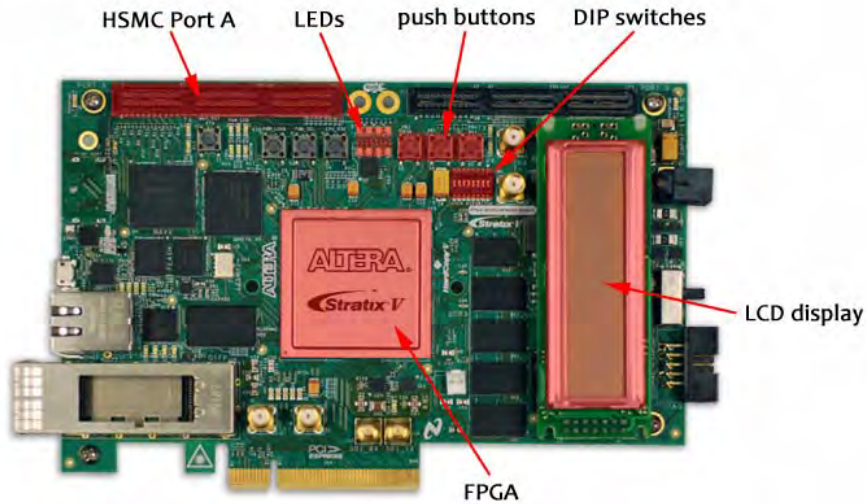
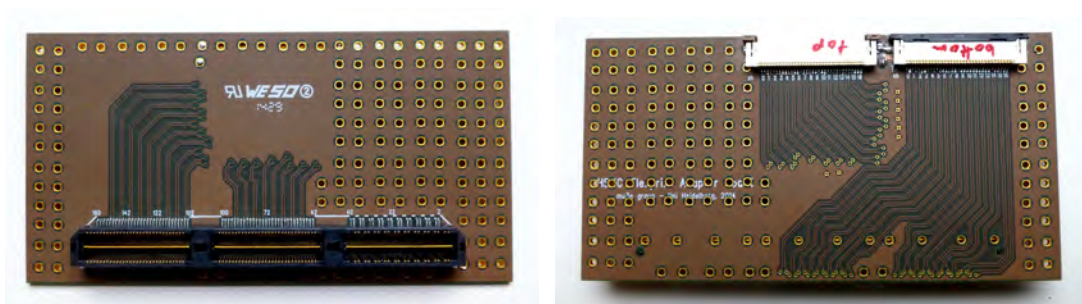


Figure 5.2: The Stratix V GX FPGA Development Board from Altera, from [71] (modified).

of the flexprints. The FPC connectors from Molex have 34 gold plated contacts with a pitch of 0.5 mm and require an FPC thickness of 0.3 mm.

For the data input and output of the development board, the HSMC port A (see Figure 5.2) suits best because it provides 17 differential LVDS pairs suitable for transmission rates up to 800 Mbit/s [70].

The pin assignment of the Stratix V allows to locate the transmitter and receiver pins in opposite rows so that a simple loopback card (see Figure 5.4) can be used to send the data directly back and test the setup even without any flexprint.



(a) Bottom side of the adapter board with an HSMC connector. (b) Top side of the adapter board with two FPC connectors.

Figure 5.3: Pictures of the HSMC Flexprint Adapter Board.

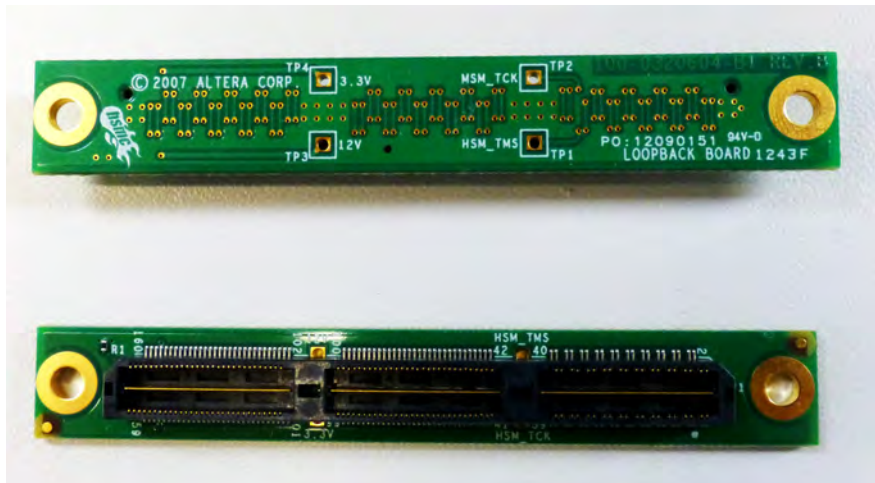


Figure 5.4: The Altera HSMC loopback board, front side and back side view.

5.2 Software

5.2.1 Altera Quartus II

Quartus II is a software package providing the complete environment needed for the design of programmable logic devices, in particular FPGAs, and can be used for the synthesis and analysis of HDL (hardware description language) designs from scratch [73].

Therefore, the logic needs to be described in VHDL [74] or Verilog HDL [75], or assembled by using a graphical interface. It is also possible to use the **MegaWizard Plug-in Manager** to input **megafunctions** which are predefined functional entities like transceivers or encoders. They can easily be configured with a graphical interface to meet the user's individual requirements.

Moreover, the input and output pins of the logic circuit can be assigned to the real physical pins of the FPGA and further options like a pre-emphasis (see Subsection 6.2.4) or differential termination can be enabled or disabled.

Also the compilation of the design is done within Quartus II. This process consists of multiple steps: After analysing the code for syntactic errors, it is synthesized and fit to the logic blocks on the FPGA considering timing constraints as well as available resources, such as memory blocks, registers, or clocks. Finally, a netlist is written which serves to be loaded on the FPGA by the **Device Programmer**. To do this, the FPGA development board can be connected to the computer via USB.

5.2.2 ModelSim

ModelSim is a software by Mentor Graphics for the simulation of the logic and timing behaviour of an HDL design [76]. All external signals, such as the position of switches or the duration of pushing a button, can be specified by the user. Therefore, ModelSim is a powerful tool to verify the logic validity of a code, especially because besides the output signals, the software also allows to display internal signals, which cannot be physically measured in practice.

5.3 Firmware: BERT Implementation

The schematic in Figure 5.5 shows the architecture of the firmware implementing the BERT. Though not shown in the figure, 17 parallel channels have been realized in the design to be able to examine crosstalk at a high trace density. In the following, the depicted components will be described part by part.

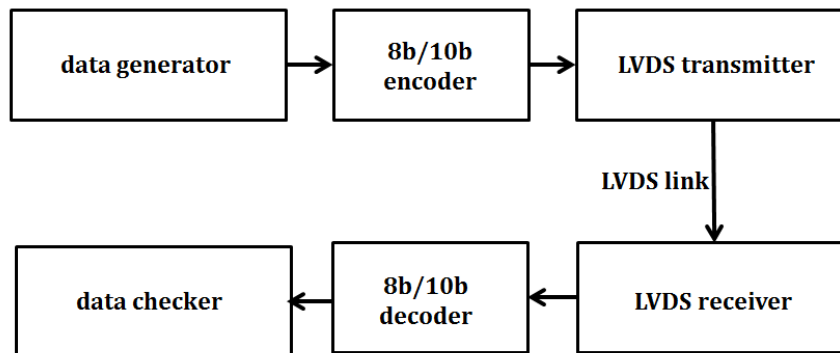


Figure 5.5: Schematic of the BERT implementation.

5.3.1 Data Generator

As 8b/10b encoding is used, it is reasonable not to exceed word lengths of 8 bits. Hence, the output data is chosen to be a simple counter from 0 to $2^8 - 1 = 255$ which increments by 1 every clock cycle and restarts from 0 when reaching the limit.

To make sure that adjacent channels do not transmit equal data, neighbouring data generators start counting from different values (see Table 5.1). Otherwise, crosstalk might possibly not lead to errors because of constructive interference.

channel no.	start value
0, 4, 8, 12, 16	$00000000_{\text{bin}} = 0_{\text{dec}}$
1, 5, 9, 13	$01000000_{\text{bin}} = 64_{\text{dec}}$
2, 6, 10, 14	$10000000_{\text{bin}} = 128_{\text{dec}}$
3, 7, 11, 15	$11000000_{\text{bin}} = 192_{\text{dec}}$

Table 5.1: Start values of the 17 data generators.

5.3.2 8b/10b Encoder

The 8b/10b encoder maps 8 bit words onto 10 bit patterns as described in Subsection 3.1.2 to achieve DC balance and ensure a high rate of transitions which is necessary for clock recovery. The encoded bitstream can be regarded as random on a short time scale, i.e. if sending less than 256 words.

It was not necessary to write an own implementation of the encoder, as a block of open source code from Critia Computer, Inc. could be inserted into the project [77].

5.3.3 LVDS Transmitter

For the transmitter, the Altera megafunction **ALTLVDS_TX** was used. It serializes the incoming 10 parallel bits from the encoder and outputs them as a differential signal. The output pins of the transmitter block are directly assigned to the physical LVDS ports of the FPGA.

The transmitter is the only entity (on the transmitter side) with an external clock input. Its output clock is fed back to all other entities on the transmitter side, namely the data generator and the encoder to guarantee synchronization.

5.3.4 LVDS Receiver

For the LVDS receiver Altera provides the **ALTLVDS_RX** megafunction which is the counterpart to the transmitter presented above. It performs clock recovery and deserializes the incoming bit stream. The recovered clock is used for all entities on the receiver side.

5.3.5 8b/10b Decoder

To recover the data from the encoded bit stream an open source code from Critia Computer, Inc. was downloaded and integrated into the project just like for the encoder [78].

5.3.6 Data Checker

Directly after booting or resetting the system, one can not immediately send user data because the transmitter and receiver are not synchronized, i.e. the receiver does not know where a 10 bit word ends and thus where to cut the bit stream. For this purpose and for clock recovery, a fixed number of K.28.5 words (see Subsection 3.1.2) is sent before the actual user data transmission begins.

Once synchronization is achieved, actual user data is transmitted. To check the incoming bit stream for errors, it is compared to the expected pattern. As the data consists of a simple counter, this can be easily implemented. Figure 5.6 shows a flow diagram of the BERT procedure.

The incoming data $D_{in}(n)$ at a clock cycle n is incremented by 1 and compared to $D_{in}(n+1)$, the data received in clock cycle $n+1$, by using the logic operation XOR. The number of ones in the resulting 8 bit string $D_{diff}(n+1)$ corresponds to the number of wrongly transmitted bits in $D_{in}(n+1)$ (presumed that $D_{in}(n)$ was correct).

If an error bit occurs and is detected correctly, $D_{exp}(n+2)$ will be wrongly calculated for the incoming data in the next clock cycle. Consequently, every error bit is counted

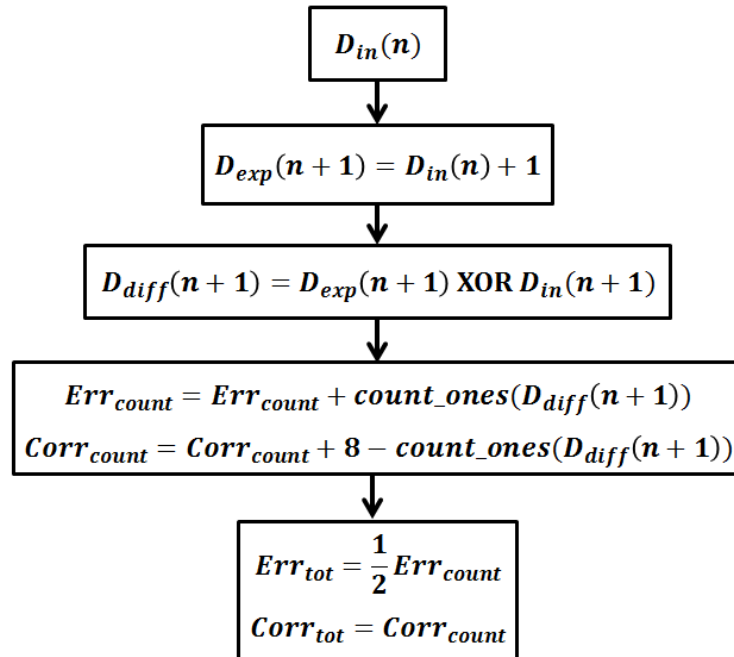


Figure 5.6: Schematic of the functionality of the data checker.

twice (see Table 5.2). Therefore, the total number of error counts Err_{count} is divided by two to get the true error number Err_{tot} .

It should be kept in mind that this test concept only works for rare errors, i.e. it does not yield reasonable results for two or more errors in a row. But since a BER far below 10^{-10} is headed for, it is appropriate to assume that there are never two subsequent error bits.

	D_{in}	D_{exp}	D_{diff}	Err_{count}
	$0_{\text{dec}} = 00000000_{\text{bin}}$	$0_{\text{dec}} = 00000000_{\text{bin}}$	00000000	0
3^{rd} bit flips:	$33_{\text{dec}} = 00100001_{\text{bin}}$	$1_{\text{dec}} = 00000001_{\text{bin}}$	00100000	1
	$2_{\text{dec}} = 00000010_{\text{bin}}$	$34_{\text{dec}} = 00100010_{\text{bin}}$	00100000	2
	$3_{\text{dec}} = 00000011_{\text{bin}}$	$3_{\text{dec}} = 00000011_{\text{bin}}$	00000000	2

Table 5.2: Example for an error being counted twice.

5.4 BERT Results

Before transmitting data via the self-manufactured flexprints, the correctness of the BERT implementation was tested by directly connecting transmitter and receiver with the help of the HSMC loopback board. Unless manually injected by using a push button, not a single error was detected independent of the frequency (100 MHz, 200 MHz, ..., 800 MHz).

After that, multiple flexprints with different trace densities, lengths and knees have been tested. The BERs can be seen in Table 5.3-5.5. The results were obtained for a data transmission at a rate of 800 Mbit/s and disabled pre-emphasis (see Subsection 6.2.4). In all shown cases not a single error has been detected. Consequently, only upper limits are given using equations 3.12 and 3.14. Broken channels, i.e. non-conducting traces, which were not carrying a proper signal but rather random noise, have been ignored for the BER calculations.

trace width w [μm]	trace separation s [μm]	distance between pairs [μm]	length [cm]	# of working channels	BER
100	150	150	10	14	$\leq 4.57 \cdot 10^{-15}$
150	150	650	10	17	$\leq 2.04 \cdot 10^{-13}$
100	150	150	20	15	$\leq 1.88 \cdot 10^{-15}$
100	150	650	30	16	$\leq 2.09 \cdot 10^{-13}$

Table 5.3: BERT results for various **coplanar striplines**.
All upper limits are given at 95% CL.

trace width w [μm]	trace separation s [μm]	distance between pairs [μm]	length [cm]	# of working channels	BER
100	150	150	10	15	$\leq 1.19 \cdot 10^{-15}$
100	150	150	20	14	$\leq 3.83 \cdot 10^{-13}$
100	150	150	30	10	$\leq 1.33 \cdot 10^{-14}$
100	150	150	30	12	$\leq 7.09 \cdot 10^{-14}$
100	150	150	30	16	$\leq 2.25 \cdot 10^{-13}$

Table 5.4: BERT results for various **differential microstrips on 25 μm Kapton**.
All upper limits are given at 95% CL.

trace width w [μm]	trace separation s [μm]	distance between pairs [μm]	length [cm]	# of working channels	BER
100	150	650	10	17	$\leq 2.76 \cdot 10^{-15}$
100	150	150	20	15	$\leq 3.68 \cdot 10^{-15}$
100	150	650	30	14	$\leq 5.05 \cdot 10^{-15}$
110	110	650	30	16	$\leq 3.28 \cdot 10^{-13}$
100	150	150	50	2	$\leq 9.44 \cdot 10^{-15}$
110	150	650	50	16	$\leq 3.07 \cdot 10^{-13}$
120	150	650	50	17	$\leq 4.14 \cdot 10^{-13}$
130	150	650	50	17	$\leq 6.12 \cdot 10^{-13}$
140	150	650	50	17	$\leq 3.02 \cdot 10^{-13}$
150	150	650	50	17	$\leq 8.31 \cdot 10^{-16}$

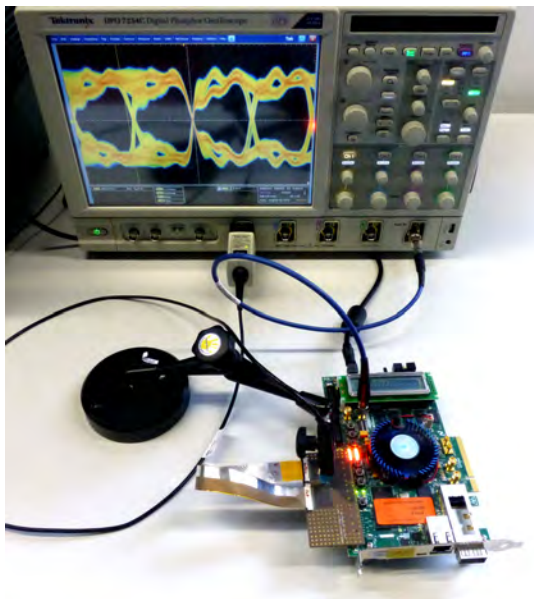
Table 5.5: BERT results for various **differential microstrips on 50 μm Kapton**.
All upper limits are given at 95% CL.

6 Analysis of Eye Diagrams

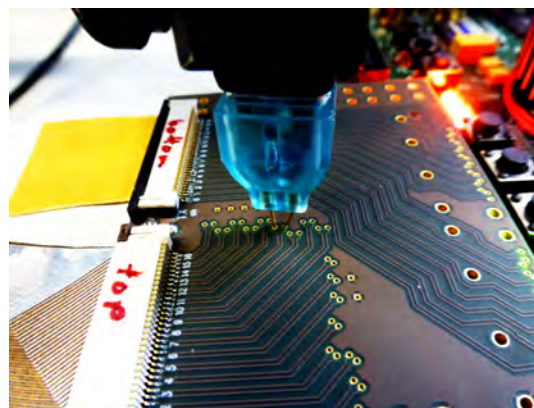
Besides the performance of BERTs, it can be valuable to analyse the signal quality of a high-speed transmission line with eye diagrams. In contrast to BERTs, which need to be run for a long time to achieve low upper limits, an eye diagram is quickly measured and allows to extrapolate the behaviour of a transmission line for higher frequencies or worse input signal qualities.

6.1 Test Setup

Basically, the same setup as for the BERTs is used. In addition, an active differential probe has been deployed to pick up the voltage signal from the adapter board and visualize it on an oscilloscope. The setup is shown in Figure 6.1.



(a) Complete setup for the measurement of eye diagrams.



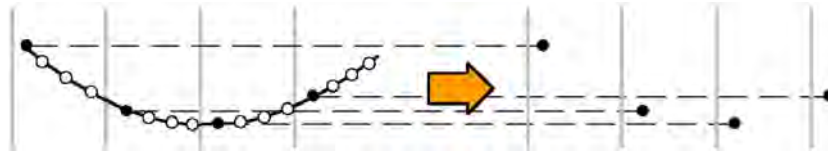
(b) Closeup of the differential probe picking up the voltage signal from a via pair on the adapter board.

Figure 6.1: Pictures showing the setup used for the measurement of eye diagrams.

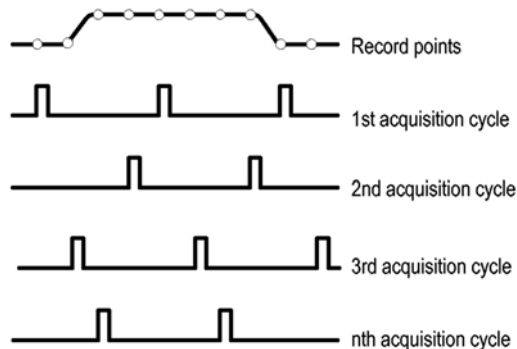
6.1.1 Tektronix DPO 7254C Digital Phosphor Oscilloscope

The Tektronix DPO 7254C Digital Phosphor Oscilloscope is a high-end oscilloscope which is suitable to analyse fast digital data transmission due to its bandwidth of 2.5 GHz and a sampling rate of 40 GS/s [79].

It provides a fast acquisition (FastAcq) mode for the analysis of dynamic signals and the capturing of rare events such as glitches. In this mode, the oscilloscope records sample points of the signal in constant time steps after being triggered as depicted in Figure 6.2a. In the next acquisition cycle it does the same with a small time shift so that after multiple acquisition cycles a complete waveform record with a very high sample density is obtained (see Figure 6.2b). By this, the sampling rate can be increased far beyond the real-time sampling rate which is limited by the shortest period between two acquisitions [80].



(a) Sample points from a single sampling process.



(b) Repetitive scanning of a waveform to obtain a very high sample density.

Figure 6.2: Schematic showing the FastAcq concept, both taken from [80].

6.1.2 Tektronix TDP3500 Differential Probe

The Tektronix TDP3500 Differential Probe is an active probe which can be connected to an oscilloscope via the TekVPI probe interface. It features very good common mode rejection and a high bandwidth of 3.5 GHz. With a very low differential input capacitance of ≤ 0.3 pF and a high input resistance of 100 k Ω it provides a high-fidelity signal reproduction for high-frequency measurements [81].

6.2 Eye Diagram Results

In the following, several parameters have been varied and compared to estimate their influence on the signal quality. If multiple eye diagrams are shown side by side, all settings and in particular the scales are equal unless explicitly stated.

In addition, the signals have been picked up from the same channel (except in 6.2.1) to achieve maximal comparability, i.e. to avoid observing the influence of different trace lengths on the adapter board.

6.2.1 Influence of the HSMC Flexprint Adapter Board

Although the adapter board was designed with a differential impedance of $100\ \Omega$, it is likely to affect the signal quality due to imperfections at its soldering points, i.e. the locations in which the HSMC connector and the FPC connectors are soldered onto the PCB. In addition, reflections certainly occur as the differential impedance of the flexprints deviate from $100\ \Omega$.

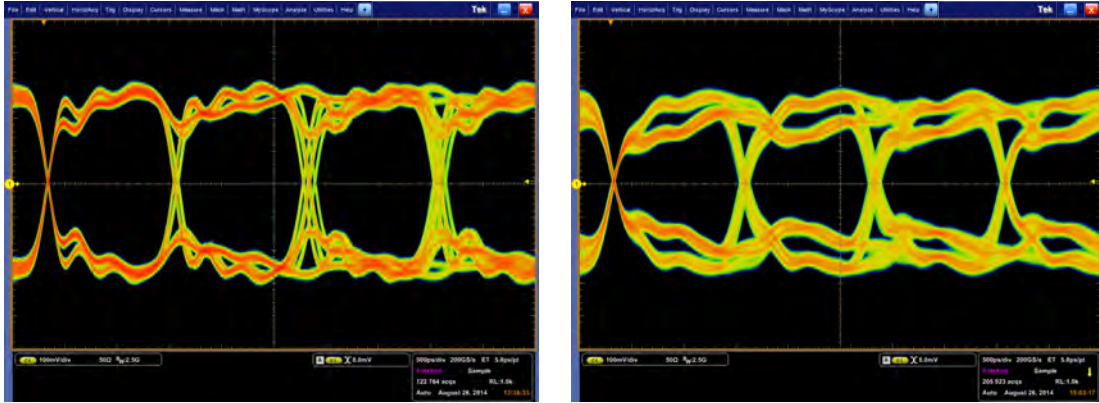
Comparison of Adapter Board and Loopback Card

Figure 6.3a depicts an eye diagram for data transmission where input and output are directly connected via the HSMC loopback card whereas the data transmission via a flexprint is shown in Figure 6.3b.

The comparison reveals that the shape of the signal is changed in some ways. A clear distinction is visible regarding the eye height which is comprehensible due to ohmic losses along the flexprint.

In both eye diagrams, one observes two slight dips shortly after a transition. But for the setup involving the loopback card, there is a strong dip nearly simultaneous with the next transition whereas the corresponding dip comes a bit later when using the adapter board and a flexprint.

It could be that the dip in Figure 6.3a is caused by reflections on the FPGA development board. Since the signal is picked up very closely to the HSMC connector in case of the loopback card but a few centimeters away on the adapter card, this might introduce a difference in the runtime of the reflected signal which leads to the observed shift of the dip. Another reason could be crosstalk between adjacent traces on the flexprint.



(a) Transmission via loopback card.

(b) Transmission via flexprint.

Figure 6.3: Eye diagrams to compare transmission involving the **loopback card** and the **adapter board**. The flexprint has a trace width of $100\ \mu\text{m}$, a trace separation of $150\ \mu\text{m}$ between all traces, a Kapton thickness of $50\ \mu\text{m}$ plus aluminum ground plane, and a length of 30 cm.

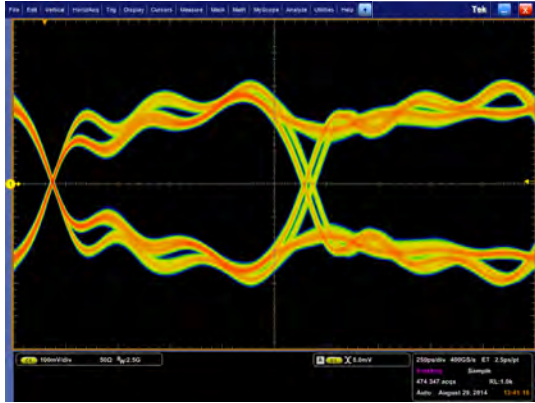
Comparison of Different Channels

The HSMC Adapter Board is not designed symmetrically and has traces of different lengths. On the transmitter side, they vary between 38.6 mm and 48.2 mm and on the receiver side between 26.2 mm and 40.0 mm, respectively.

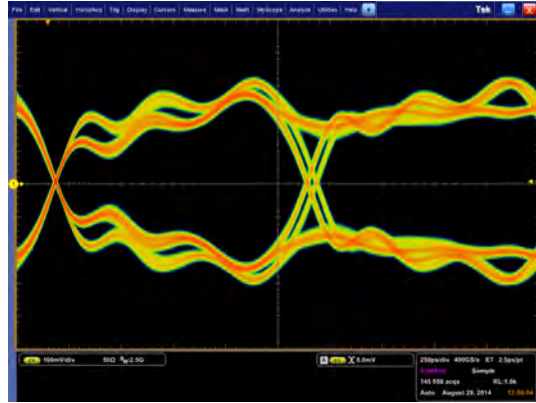
For the eye diagrams in Figure 6.4, the signal has been picked up at channels 0, 11 and 16. Since the traces on the flexprint might slightly differ in trace thickness or separation due to production tolerances, for the eye diagrams in the right column the flexprint has been connected with interchanged ends (see Figure 6.5). I.e. different channels have been compared using exactly the same differential pair on the flexprint for maximal comparability.

It can be seen that interchanging the ends of the flexprint makes only a very slight difference, which could be introduced by an improper connectivity to the FPC connector. On the contrary, there is a strong disparity when comparing the different channels.

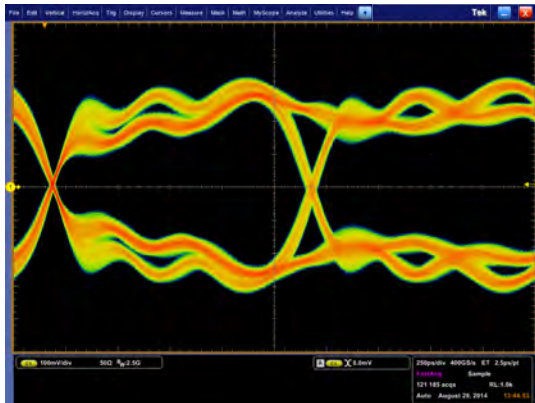
For the flexprint used in this comparison it can be assumed that the reflections at the HSMC connector dominate the total reflections on the receiver side because these are of first order, whereas reflections caused by an improper impedance matching of the flexprint are of second order or higher (see Figure 6.6). Therefore, it is likely that the differences between the eye diagrams seen in Figure 6.4 are primarily caused by different runtimes of the reflections due to different trace lengths on the receiver side of the PCB and possibly also on the FPGA development board.



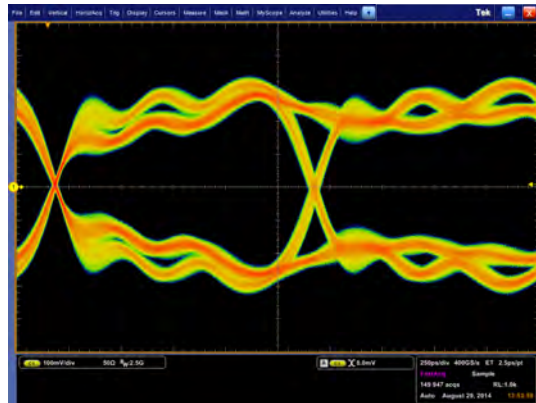
(a) Channel 0. PCB trace length at transmitter/receiver side: 46.1 mm/26.2 mm.



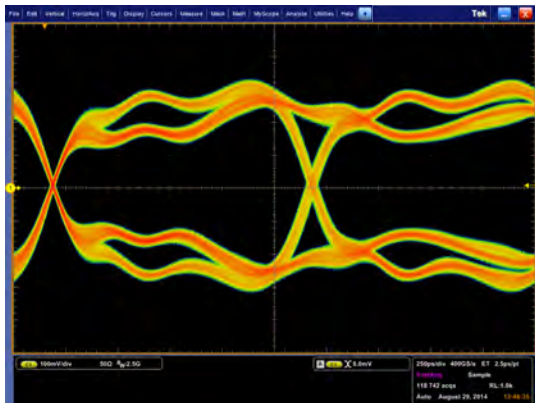
(b) Channel 0. Flexprint connected with interchanged ends.



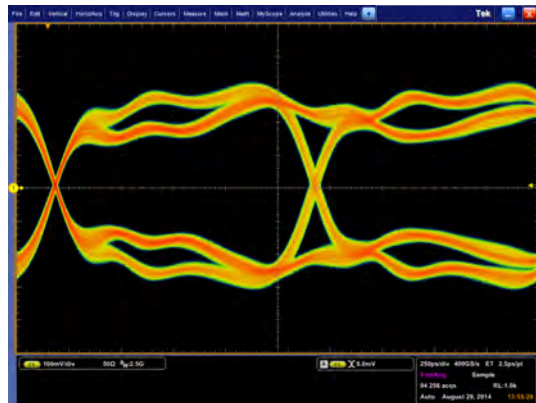
(c) Channel 11. PCB trace length at transmitter/receiver side: 38.7 mm/35.54 mm.



(d) Channel 11. Flexprint connected with interchanged ends.



(e) Channel 16. PCB trace length at transmitter/receiver side: 40.7 mm/40.0 mm.



(f) Channel 16. Flexprint connected with interchanged ends.

Figure 6.4: Eye diagrams picked up at **different channels**. 800 Mbit/s transmission via a flexprint with a trace width of $100\ \mu\text{m}$, a trace separation of $150\ \mu\text{m}$ for pairs and $650\ \mu\text{m}$ between pairs, and a Kapton thickness of $50\ \mu\text{m}$ plus aluminum ground plane. Length: 10 cm.

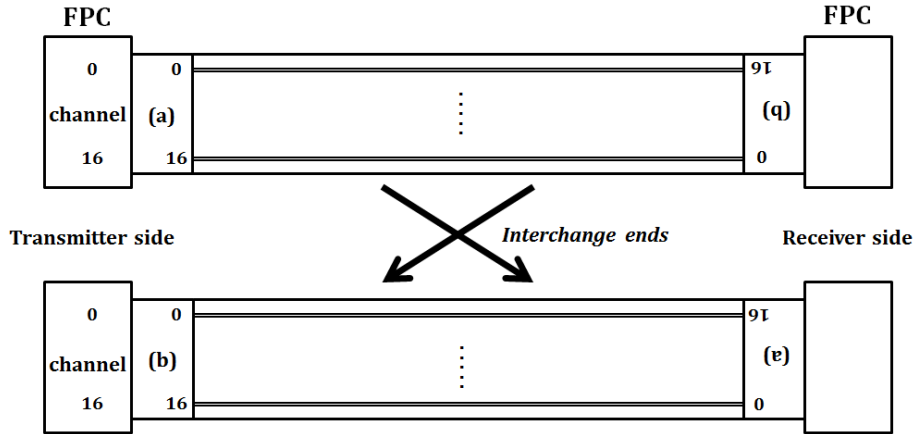


Figure 6.5: Interchange of the ends of the flexprint for maximal comparability.

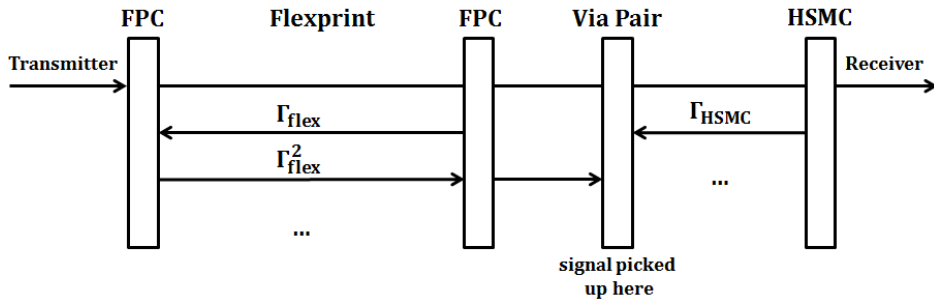
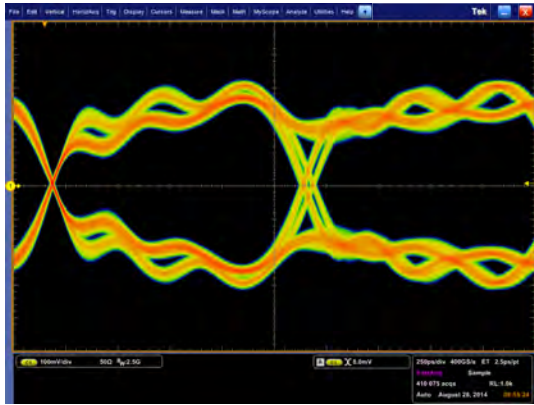


Figure 6.6: Schematic of the reflections at the FPC and the HSMC connectors. Γ_{flex} can be calculated with equation 3.4, Γ_{HSMC} is not known.

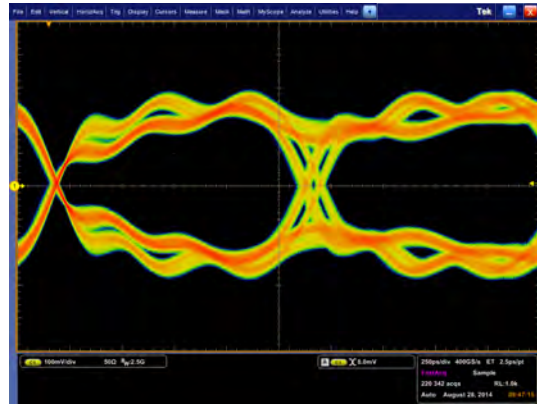
6.2.2 Influence of the Cable Length

To estimate the influence of the cable length on the signal quality, three flexprints with different lengths are compared in Figure 6.7.

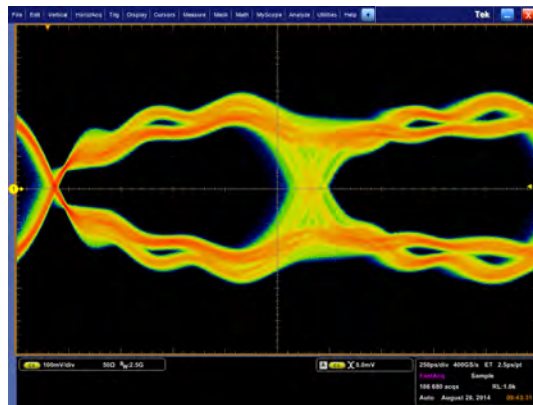
As can be seen, the length does not affect the qualitative shape of the eye. In all cases, there are basically two dips after a transition. This supports the theory that the reflections due to improper impedance matching of the flexprint do not dominate the total reflection. In fact, one would expect different signal shapes because of different runtimes of the reflected signals unless the cable lengths equal multiples of the wavelength. This is unlikely since with a base frequency of 400 MHz and a propagation velocity of approximately 2/3 of the speed of light, the wavelength should be roughly 50 cm.



(a) Length: 10 cm.



(b) Length: 20 cm.



(c) Length: 30 cm.

Figure 6.7: Eye diagrams of 800 Mbit/s data transmission via flexprints with a trace width of $100\ \mu\text{m}$, a trace separation of $150\ \mu\text{m}$ for pairs and $650\ \mu\text{m}$ between pairs, and a Kapton thickness of $50\ \mu\text{m}$ plus aluminum ground plane, but **different lengths**.

As the signal deformation is independent of the cable length, one can rather proceed on the assumption that reflections at the flexprint are not even visible in these eye diagrams.

However, one observes that there is an attenuation of the signal which grows with the cable length. This meets the expectation since the ohmic resistance of the aluminum traces rises with their lengths.

In addition, the jitter is enhanced for the longer cables. Nevertheless, the basic eye shape is conserved and the signal transmission works properly.

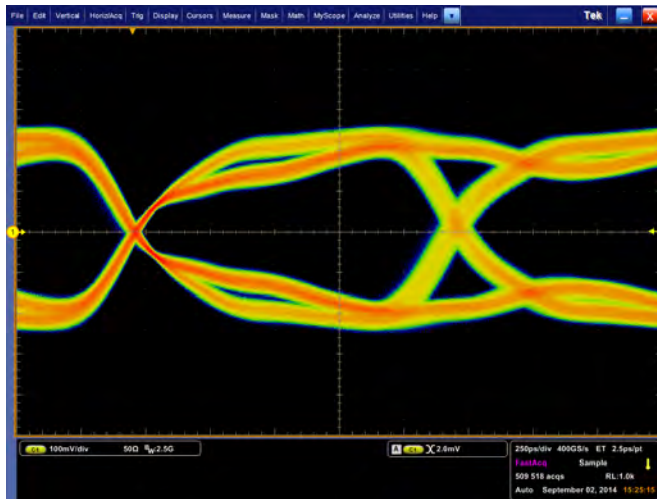


Figure 6.8: Eye diagram of an 800 Mbit/s data transmission via a flexprint with a **trace width and a trace separation of 150 μm** , a Kapton thickness of 50 μm plus aluminum ground plane, and a **length of 50 cm**.

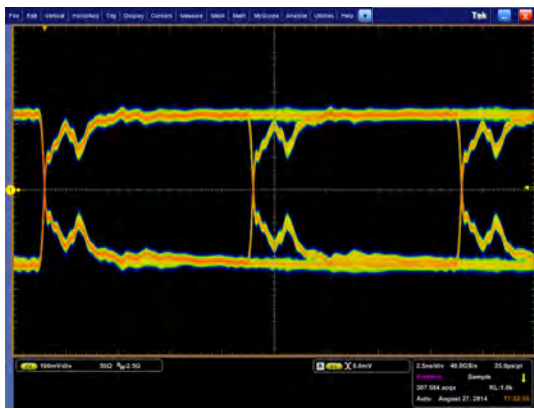
Another eye diagram, which is shown in Figure 6.8, has been recorded for a 50 cm flexprint. In contrast to the flexprints discussed above, it had a trace width and a trace separation of 150 μm .

Compared to the eye diagrams in Figure 6.7 one observes a further decrease of the eye height and less distinct dips. This meets the expectations due to higher ohmic losses caused by the length. Surprisingly, the amount of jitter is reduced towards the 30 cm flexprint in Figure 6.7c, but a reason for this observation could not be found.

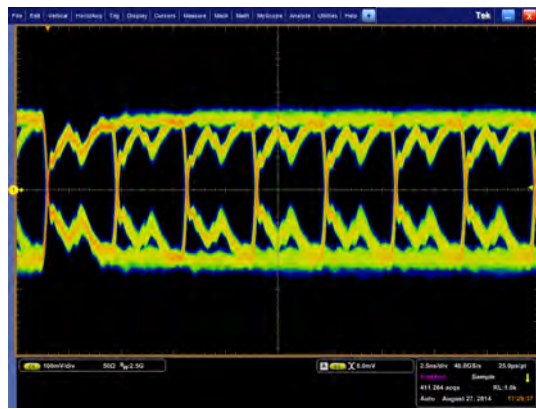
6.2.3 Influence of the Transmission Rate

In Figure 6.9, eye diagrams for different transmission rates are depicted. In all four cases, one observes two slight dips before a strong dip appears approximately 1.7 ns after a transition, followed by further slight dips.

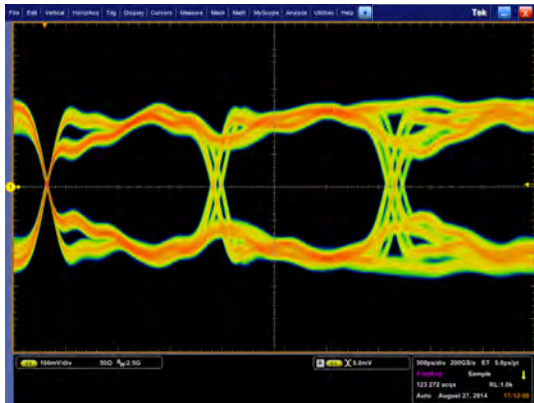
Since the eye shape does not depend on the cable length, as seen in Subsection 6.2.2, it is likely that this strong dip occurs because reflections at the HSMC connector on the receiver side run back to the via pair where the signal is picked up.



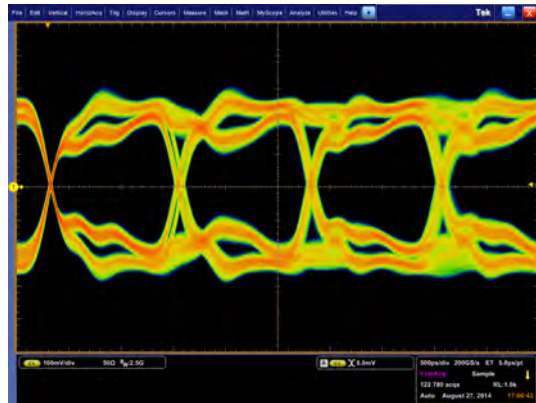
(a) Transmission rate: 100 Mbit/s. x-axis: 2.5 ns/div.



(b) Transmission rate: 300 Mbit/s. x-axis: 2.5 ns/div.



(c) Transmission rate: 600 Mbit/s. x-axis: 500 ps/div.



(d) Transmission rate: 800 Mbit/s. x-axis: 500 ps/div.

Figure 6.9: Eye diagrams of data transmission at **different rates** via flexprints with a trace width of $100 \mu\text{m}$, a trace separation of $150 \mu\text{m}$ between all traces, and a Kapton thickness of $50 \mu\text{m}$ plus aluminum ground plane. Length: 20 cm.

The slight dips might come from a limited bandwidth of the transmitter since they appear independent of the frequency and even when using the loopback card (see Figure 6.3a) so that they are definitely not caused by the flexprint or the adapter board.

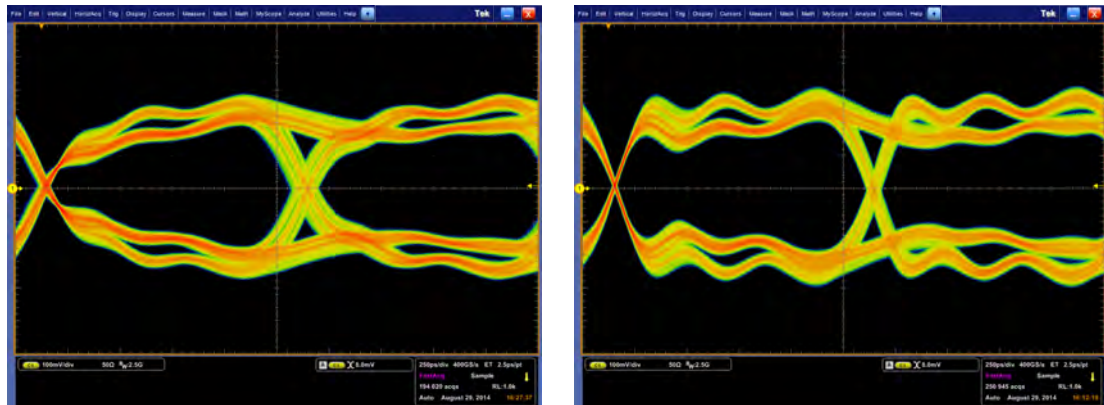
Besides, the slew rate is observed to be equal for all frequencies which indicates that it is limited by the transmitter. Also, the eye height does not change with the frequency.

Even though the frequency could not be increased beyond 800 Mbit/s due to limitations of the transmitter, the signal shape allows to assume that the flexprints would also work at higher transmission rates because the deformation of the signal does not show any frequency dependence and the bit states are always clearly distinguishable.

6.2.4 Influence of the Pre-Emphasis

At high frequencies, the slew rate of the transmitter is not fast enough to reach the full voltage level before the next transition. This conduces to a pattern dependent jitter because the edge of a transition comes a bit earlier if the full voltage level has not been reached yet.

To minimize this jitter, the amplitude of the high-frequency components of the output signal can be enhanced. This so-called **pre-emphasis** leads to a voltage overshoot shortly after a transition and increases the slew rate [67].



(a) Pre-emphasis disabled.

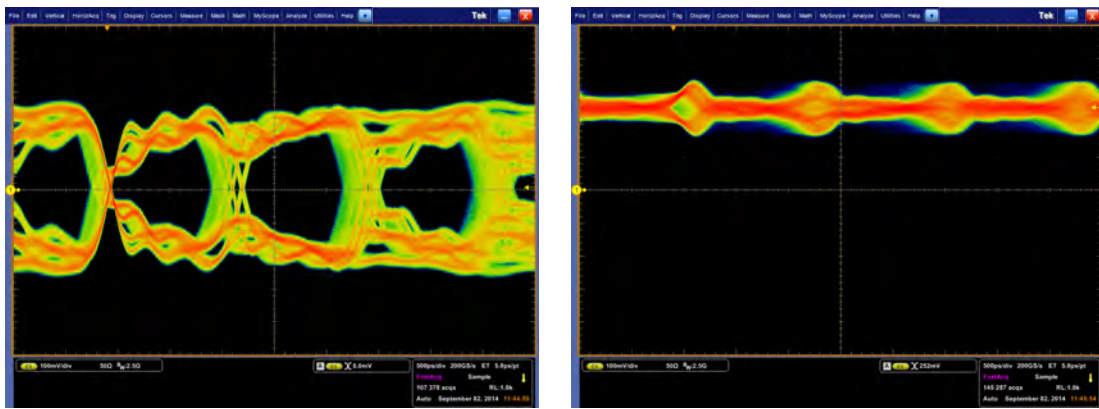
(b) Pre-emphasis enabled.

Figure 6.10: Eye diagrams showing the effect of enabled **pre-emphasis**. The flexprint has a trace width of $100\ \mu\text{m}$, a trace separation of $150\ \mu\text{m}$ between all traces, a Kapton thickness of $25\ \mu\text{m}$ plus aluminum ground plane, and a length of 30 cm. Transmission rate: 800 Mbit/s.

Figure 6.10 depicts the change in the signal shape due to enabled pre-emphasis. The overshoot and an increased slew rate are clearly recognisable. Especially in the first quarter, the eye opening is notably larger. Furthermore, it can be seen that the amount of jitter is reduced.

6.2.5 Crosstalk between Trace Pairs

To examine how much noise is induced on an adjacent trace pair, the firmware was slightly changed so that only every second channel was used for data transmission and the intermediate trace pairs were not assigned to FPGA pins.

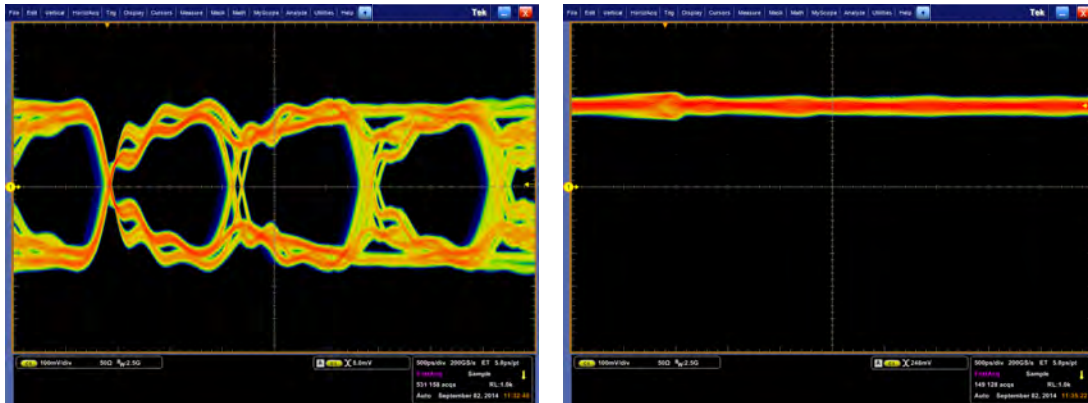


(a) Signal on channel 0.

Kapton thickness: 25 μm , no ground plane.

(b) Induced signal on channel 1.

Kapton thickness: 25 μm , no ground plane.



(c) Signal on channel 0.

Kapton thickness: 50 μm plus ground plane.

(d) Induced signal on channel 1.

Kapton thickness: 50 μm plus ground plane.

Figure 6.11: Eye diagrams showing **crosstalk** for different Kapton thicknesses. Data transmission at 800 Mbit/s via flexprints with a trace width of 100 μm , a trace separation of 150 μm between all traces, and a length of 20 cm.

For the eye diagrams in the right column of Figure 6.11, the signal was picked up at an unassigned trace pair between two properly working channels. One observes that crosstalk is present for both types of flexprints, i.e. for coplanar striplines as well as for differential microstrips. But in case of the coplanar striplines, there is a clear periodic structure in the induced signal whereas for the differential microstrips it is mostly flat and thus interpreted as noise.

Moreover, the amplitude of the induced signal is much larger for the coplanar striplines. This means that the aluminum ground plane really effectively shields the adjacent channels and decreases the amount of crosstalk.

6.2.6 Influence of the Microstrip Type

In Figure 6.12, eye diagrams for different microstrip types can be seen. The comparison shows that the eye diagrams clearly differ regarding the band thicknesses. The bands in the signal for the coplanar striplines (Figure 6.12a) are notably widened and also the amount of jitter is increased. On the other hand, the two signals for the differential microstrips with different Kapton thicknesses (Figures 6.12b and 6.12c) do not significantly deviate from each other.

This is comprehensible when regarding the results from Subsection 6.2.5. In case of the coplanar striplines the amount of crosstalk is much larger than for the differential microstrips since the aluminum ground plane effectively shields adjacent trace pairs and minimizes crosstalk.

In contrast, the basis eye shape does not differ. In all three cases, there are two slight dips after a transition and for those bands remaining at a logic level for longer than one unit interval, there is another stronger dip somewhat after the next transition. Furthermore, all dips are nearly of equal intensity.

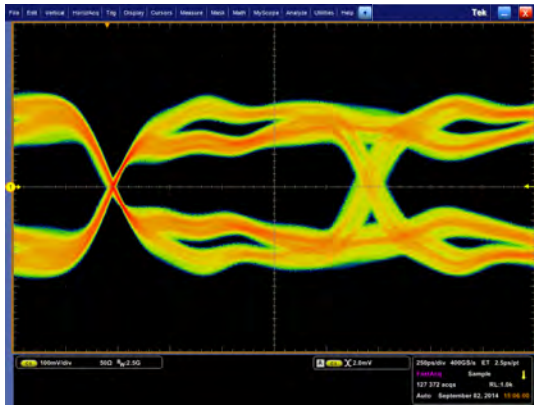
In Subsection 6.2.2, it has been seen that the signal deformation for differential striplines on 50 μm Kapton (with ground plane) are not dependent on the length, except for the attenuation of the amplitude. This led to the conclusion that reflections due to improper impedance matching are not observable in the eye diagram.

Since the intensity of the dips does not notably differ for the different microstrip types, it is likely that the effect of impedance matching is negligible in all three cases.

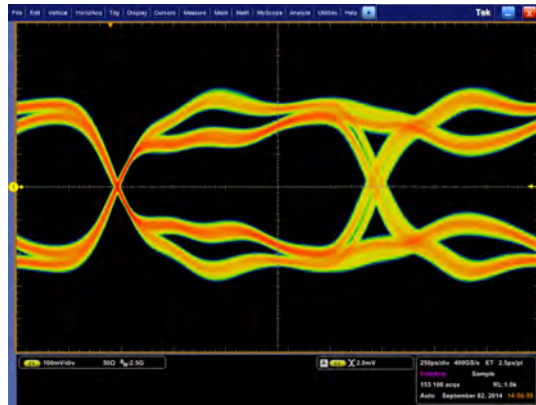
To support this theory, the runtime of the reflected signals are estimated: The distance, the signal has to run, comprises twice the cable length of 20 cm and a trace length of 4 mm from the FPC connector to the via pair where the signal is picked up.

A propagation velocity of $2/3$ of the speed of light and a base frequency of 400 Mbit/s result in a runtime of approximately 2 ns. But 2 ns after the transition in Figures 6.12a-c no specific dip can be observed.

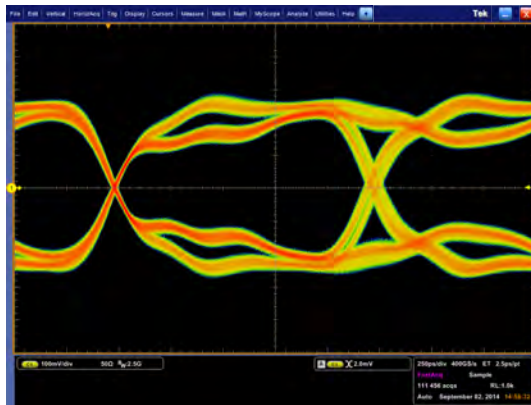
Therefore, it can be concluded that the impedance matching is only of minor importance for the eye shape and crosstalk affects the signal quality much more.



(a) **Coplanar Stripline.** Kapton thickness: $25\ \mu\text{m}$ without ground plane, calculated $Z_{\text{diff}} \approx 268\ \Omega$.



(b) **Differential Microstrip.** Kapton thickness: $25\ \mu\text{m}$ on ground plane, calculated $Z_{\text{diff}} \approx 40\ \Omega$.



(c) **Differential Microstrip.** Kapton thickness: $50\ \mu\text{m}$ on ground plane, calculated $Z_{\text{diff}} \approx 90\ \Omega$.

Figure 6.12: Eye diagrams of 800 Mbit/s data transmission via flexprints with a trace width of $100\ \mu\text{m}$, a trace separation of $150\ \mu\text{m}$ between all traces, and a length of 20 cm, but **different microstrip types**.

6.2.7 Influence of the Knee Length

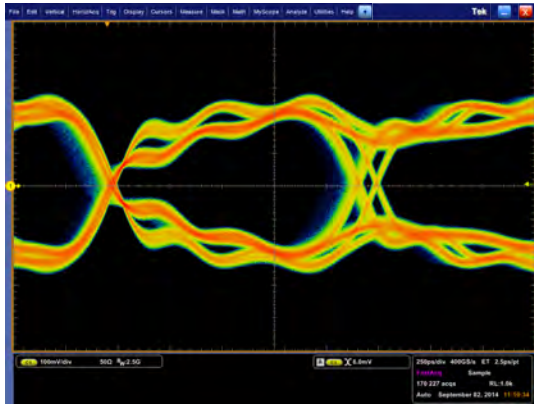
For flexprints with a trace separation of $150\ \mu\text{m}$ between all traces, there is a spread at both ends to meet the $0.5\ \text{mm}$ pitch of the FPC connectors. The question arises whether the length of the knees (i.e. the sections running 45° to the main section) notably impair the signal quality because here the trace thickness and separation deviate from the main section and the edges of the traces are less smooth (see Figures 4.5b and 4.6b).

To estimate this influence, channels 0, 8 and 16, i.e. the channel with no knee at all, a mean knee length, and the one with the longest knee, are compared in Figure 6.13. Again, the flexprint is connected with interchanged ends in the right column to distinguish the influence of the knee from the intrinsic differences of the channels (see Figure 6.14).

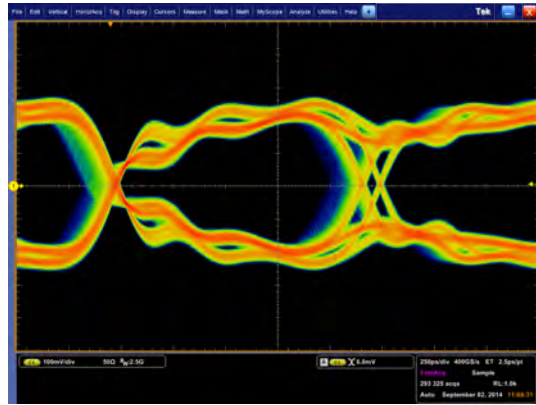
The eye diagrams for channel 8 should and do look exactly the same in both cases since 8 is in the middle of 17 and the direction of the data transmission should make no difference due to the symmetric structure of the cable.

Also the other eye diagrams for no knee and the maximal knee length look fine. The comparison of Figures 6.13a and 6.13b shows that there is only a very slight difference in the height of the wiggles, whereas the basic signal shape is conserved. The amount of jitter does not notably differ. The same is observed in Figures 6.13e and 6.13f.

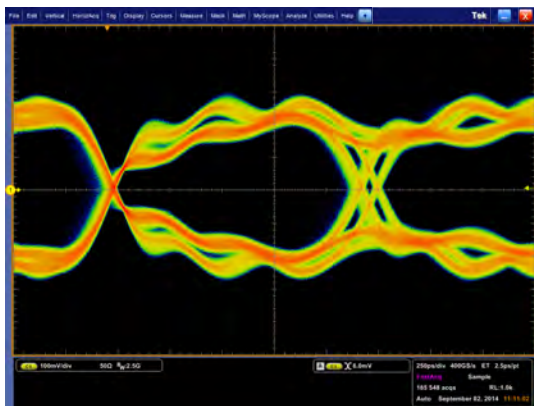
Consequently, the influence of the knee length can be considered to be of minor importance and the use of 45° sections in a flexprint does not significantly impair the signal quality.



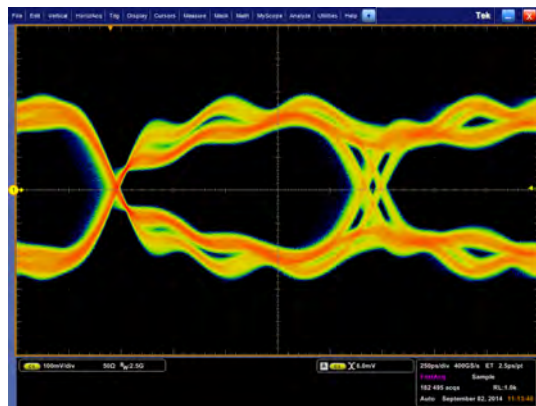
(a) No knee (channel 0).



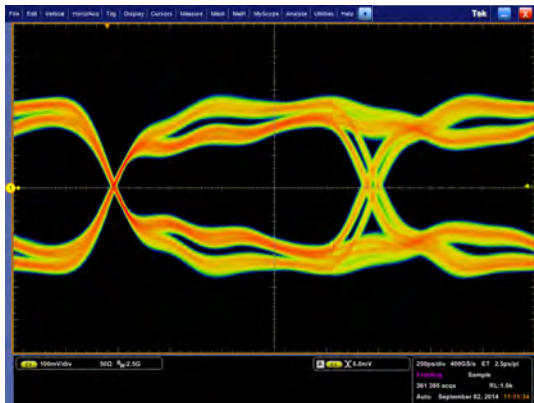
(b) Maximal knee length (channel 0). Flexprint connected with interchanged ends.



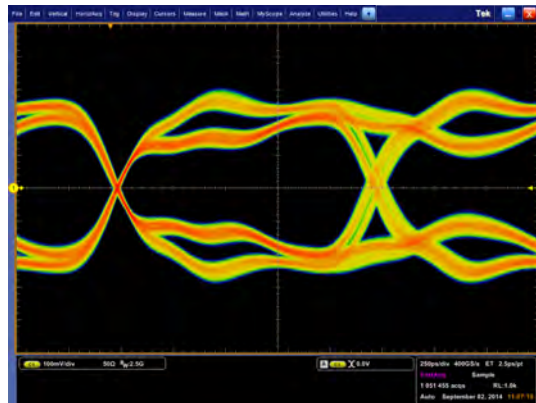
(c) Medium knee length (channel 8)



(d) Medium knee length (channel 8). Flexprint connected with interchanged ends.



(e) Maximal knee length (channel 16).



(f) No knee (channel 16). Flexprint connected with interchanged ends.

Figure 6.13: Eye diagrams for different knee lengths. 800 Mbit/s transmission via a flexprint with a trace width of $100\ \mu\text{m}$, a trace separation of $150\ \mu\text{m}$ between all traces, and a Kapton thickness of $50\ \mu\text{m}$ plus aluminum ground plane. Length: 10 cm.

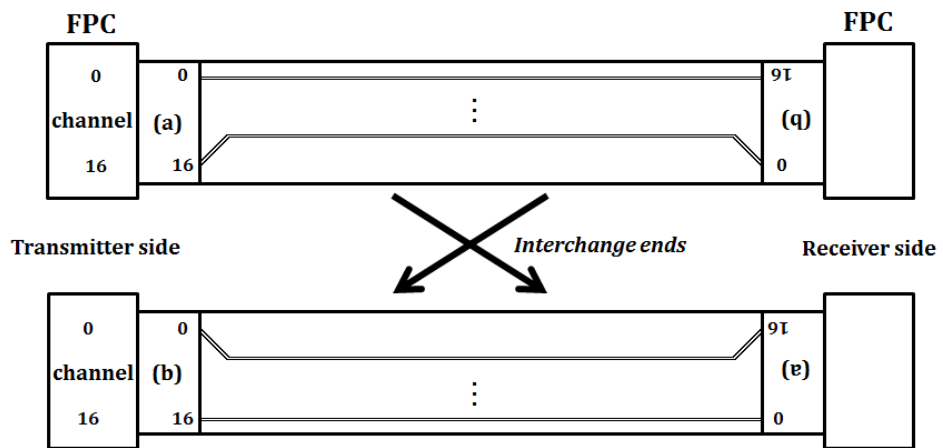


Figure 6.14: Interchange of the ends of the flexprint to compare different knee lengths using the same channel.

Part III

Conclusion & Outlook

7 Conclusion

For this thesis, Kapton flexprints have been produced with a laser system at the Heidelberg University for the Mu3e experiment. Bit Error Rate Tests (BERTs) at a transmission rate of 800 Mbit/s have been performed which resulted in upper limits for the bit error rates below $O(10^{-15})$. Furthermore, eye diagrams have been analyzed to understand which factors mainly affect the signal quality.

7.1 Manufacturing of Kapton Flexprints

It has been shown that flexprints with a (horizontal) trace width and a trace separation of $\geq 120 \mu\text{m}$ can be manufactured with a high reliability, i.e. without any broken traces. These can also be combined with 45° sections and vertical sections of traces with a width of $\geq 150 \mu\text{m}$. The vertical sections should rather be short and can be used as pads to connect the flexprints to the FPC connectors.

Also flexprints with smaller (horizontal) trace widths down to $100 \mu\text{m}$ can be manufactured but show broken traces (mostly 1-3 in 34, sometimes more).

With the used laser platform, it is not possible to go below a trace separation of $100 \mu\text{m}$ which corresponds to the width of the laser focus. It is problematic to use small trace separations in a design because the laser changes its mode from 'rastering' to 'vectoring' for a separation of $\leq 100 \mu\text{m}$ and an offset or imprecision introduced by the mechanics of the laser platform leads to inaccurate traces.

This means that the production of flexprints is limited to be done with a single laser setting for 'rastering'. 'Vectoring' is only suited to cut out the flexprint.

It has also been shown that differential microstrips can be realized by gluing a flexprint and an unprocessed piece of Kapton laminated with aluminum of the same shape together. This can be done with both sides of the Kapton-aluminum foil so that differential microstrips with a Kapton thickness of $25 \mu\text{m}$ plus adhesive layer or $50 \mu\text{m}$ plus adhesive layer can be obtained. The influence of different Kapton thicknesses on the impedance matching and crosstalk was examined and measurements were performed.

Possible reasons for the blackening of the Kapton due to the processing with the laser have been discussed. According to the interpretation given, the laser treatment does not significantly change the dielectric properties of the Kapton to the detriment of the experiment.

7.2 BERT Results

BERTs have been performed that have shown that data transmission works flawlessly for a variety of flexprints. Even coplanar striplines without a ground plane can be used for an errorless data transmission though the signal quality is worse in comparison to differential microstrips (see Section 7.3).

7.3 Eye Diagram Results

The analysis of multiple eye diagrams has lead to the following results:

- The signal deformations which can be observed in the eye diagrams are neither dependent on the transmission rate nor on the flexprint length. The shape even resembles the signal picked up from the loopback card alone. Therefore, the signal deformations are unlikely to be caused by reflections at the FPC connectors due to improper impedance matching. Consequently, a differential impedance for flexprints of the type 'differential microstrips' in the range of 40-60 Ω seems sufficient to minimize the reflections to an acceptable level.
- Comparing flexprints of different lengths has shown that the eye height decreases with increasing cable length. Nevertheless, also for 50 cm flexprints, the signal shape allows a clear distinction between the logic states.
- The signal shape looks much better for flexprints of the type 'differential microstrips' than 'coplanar striplines'. The additional aluminum ground plane decreases crosstalk effectively and possibly also improves impedance matching. Moreover, it provides space for ground and power supply which would have to be placed on the flexprint itself in case of 'coplanar striplines'. Even though it increases the material budget, the amount of scattering is notably reduced in comparison to leading-edge flexprints applying copper (see Section 4.3).
- An enabled pre-emphasis enhances the signal quality and increases the slew rate of the signal. Nevertheless, also without this option enabled a flawless data transmission is possible at 800 Mbit/s. Although pre-emphasis involves further electronics,

namely an additional LVDS driver, which leads to a higher power consumption, this option is foreseen on the final Mupix chip [82].

7.4 Recommendations

In the present work, it could be shown that it is possible to produce Kapton flexprints with the PLS6MW Multi-Wavelength Laser Platform and transmit data at a rate of 800 Mbit/s with a BER below $O(10^{-15})$ at 95% CL.

A proper trace separation works down to 110 μm and the trace width can be decreased down to 100 μm . However, it has been observed that this minimal trace width leads to broken traces and is therefore not suitable for mass production with the used laser platform, whereas for trace widths $\geq 120 \mu\text{m}$ the connectivity is reliable. In addition, it has been seen that a ground (or other constant potential) plane notably improves the signal quality.

Based on these results, the following recommendations (see also Table 7.1) can be made:

Since a reliable connectivity of the traces is crucial, a trace width of 120 μm is recommended. This can be combined with a trace separation of 110 μm . For traces which are routed with an angle of 45° to the main section an increased trace width and trace separation of each 150-175 μm should be used. Also structures perpendicular to the main direction can be included in the design but should rather be used as pads for the connection of FPC plugs or the like.

An additional aluminum plane improves the signal quality and delivers more space for power supply and ground so that it should be used for the Mu3e experiment even though it slightly increases the material budget.

	trace width [μm]	trace separation [μm]
horizontal	120	110
45°	≥ 150	≥ 150
vertical	≥ 150	≥ 150

Table 7.1: Recommended structure sizes for the Mu3e experiment.

8 Outlook

8.1 Consequences for the Mu3e Experiment

8.1.1 Spatial Constraints

When regarding the spatial constraints of the Mu3e detector, the structure sizes shown in Table 7.1 are sufficient for flexprints to connect the Mupix chips to the front-end FPGAs:

The inner double layer will have a polygonal shape with an active length of 12 cm consisting of 12 and 18 sides, respectively. Since the final chip size of the Mupix chips will be $1 \times 2 \text{ cm}^2$ in the inner region, 6 chips will be used on every side of which 3 will be connected upstream and 3 downstream. Each of these chips will have 3 LVDS output ports.

Consequently, 9 parallel LVDS channels need to be placed on one flexprint. A trace width of $120 \mu\text{m}$ and a trace separation of $110 \mu\text{m}$ lead to a total width of 0.414 cm for the horizontal section. Since each chip has a length of 2 cm , there will be an area of $0.586 \times 2 \text{ cm}^2$ to spread the traces using 45° sections and place bonding pads.

Ground and power could be supplied by integrating holes in the Kapton to be able to bond on the underlying ground/power plane as depicted in Figure 8.1. For this purpose, differential microstrips on $25 \mu\text{m}$ Kapton would be much easier to produce than on $50 \mu\text{m}$ because in case of the latter, one would need to find a way to partially remove the Kapton from the aluminum to bond to the underlying metal plane.

These structure sizes also suffice for the outer polygonals which will have a length of 36 cm and 24-26 sides with a width of 2 cm . Here, the chips will have a size of $2 \times 2 \text{ cm}^2$ so that 18 chips will be mounted in a row. These will have only 1-2 LVDS output channels so that to each side ≤ 18 channels need to be placed on a 2 cm wide flexprint. This is at most as narrow as in the inner layers and should work as well [10].

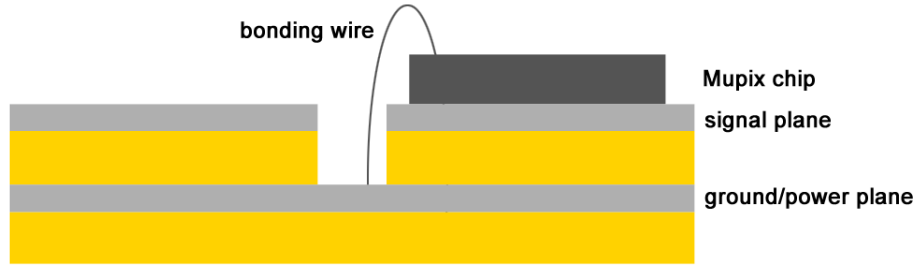


Figure 8.1: Schematic showing the concept of bonding on the underlying aluminum plane.

8.1.2 Transmission Errors

In phase I of the Mu3e experiment, 180 chips with 3 LVDS output channels each will be used in the innermost double layer. The outer double layer will mount 972 chips with 1-2 channels each so that the total number of channels adds up to ≤ 2142 [10].

With a $\text{BER} \leq 10^{-15}$ at 95% CL and equation 3.12 the mean time τ for an error to occur can be estimated:

$$\text{BER} = \frac{\# \text{ errors}}{\# \text{ total bits}} \stackrel{!}{=} \frac{1}{800 \text{ Mbit/s} \cdot \# \text{ channels} \cdot \tau} \quad (8.1)$$

$$\Rightarrow \tau \geq 86 \text{ min.} \quad (8.2)$$

Note that the "true" value for τ might be much larger because no error bit has been observed.

Since the pixel detectors will be read out in time frames of 50 ns (see Subsection 2.1.3), this means that only a very small fraction of $\leq 10^{-11}$ of the readout frames will contain an error bit (if at all) whereas it is very unlikely that two error bits occur in the same frame. The firmware or software should be able to detect a single error bit so that such an unemployable readout frame can be discarded. Due to the very low rate of frames containing error, this would not harm the experiment.

8.2 Further Work

Several tasks are left which must be focused on in subsequent works. These are:

- The flexprints which have been produced so far did only act as test cables to show that data transmission at 800 Mbit/s works in principle and to find out suitable trace widths and trace separations which can be manufactured reliably.

Further investigations have to be done on flexprint designs which really fit the Mupix chips and the spatial constraints in the detector.

- It has been seen, that an aluminum ground plane notably increases the signal quality since it suppresses crosstalk between adjacent trace pairs and (presumably) also enhances impedance matching.

Still, it has the drawback of an increased material budget which leads to stronger multiple scattering. It should be tested whether a thinner aluminum thickness of $< 12 \mu\text{m}$ can function as a ground (or power) plane.

- Research has to be done on the question how to bond the Mupix chips to the Kapton flexprints.
- So far, no statement could be made about the lifetime of the Kapton flexprints. The aluminum might possibly suffer from oxidation which could decrease the conductivity to the FPC connectors or make it more vulnerable to bending since aluminum oxide is a brittle material.

List of Figures

1.1	Particles described by the SM	3
1.2	Feynman diagrams of possible SM muon decays	4
1.3	Feynman diagrams of possible BMS muon decays	4
1.4	The history of LFV muon decay experiments	5
2.1	The internal conversion decay $\mu^+ \rightarrow e^+e^-e^+\nu_\mu\bar{\nu}_e$	7
2.2	Branching ratio for the internal conversion as a function of the missing energy	7
2.3	Possible combinatorial background	8
2.4	Schematic drawing of the detector design	9
2.5	First mechanical prototype of the Kapton support structure for the inner two layers	10
2.6	Schematic of the Mu3e readout chain	12
3.1	Basic LVDS circuit	14
3.2	Binary datastream and corresponding voltage	15
3.3	Two commonly used line codes	16
3.4	Equivalent circuit diagram of a short piece of a transmission line	18
3.5	Profiles of differential microstrips and coplanar striplines	20
3.6	An ideal and a real arbitrary digital datastream and their eye diagrams	23
3.7	A typical eye diagram with key parameters	24
4.1	PLS6MW Laser Platform	26
4.2	Dependence of the dielectric constant ϵ_r on various quantities	28
4.3	Test structures to examine which minimal structure sizes can be achieved by rastering	33
4.4	Flexprint type 1	34
4.5	Flexprint type 2	35
4.6	Flexprint type 3	36
4.7	Attempt to cut a single trace into two thin traces	37
4.8	Photo showing the thickened ends of two flexprints	38
4.9	Microscopic images of flexprints showing the blackening of the processed Kapton	40
5.1	Picture showing the setup comprising the FPGA development board, the HSMC adapter board and the self-manufactured flexprint	42
5.2	Stratix V GX FPGA Development Board	44
5.3	HSMC Flexprint Adapter Board	44
5.4	Altera HSMC loopback board	45

5.5	Schematic of the BERT implementation	46
5.6	Schematic of the functionality of the data checker	48
6.1	Pictures showing the setup used for the measurement of eye diagrams	51
6.2	Schematics showing the FastAcq concept	52
6.3	Eye diagrams to compare the transmission involving the loopback card and the adapter board	54
6.4	Eye diagrams picked up at different channels	55
6.5	Interchange of the ends of the flexprint for maximal comparability	56
6.6	Schematic of the reflections at the FPC and the HSMC connectors	56
6.7	Eye diagrams for different cable lengths	57
6.8	Eye diagram for a 50 cm long flexprint	58
6.9	Eye diagrams at different transmission rates	59
6.10	Eye diagrams showing the effect of enabled pre-emphasis	60
6.11	Eye diagrams showing crosstalk for different Kapton thicknesses	61
6.12	Eye diagrams for Kapton thicknesses	63
6.13	Eye diagrams for different knee lengths	65
6.14	Interchange of the ends of the flexprint to compare different knee lengths using the same channel	66
8.1	Schematic showing the concept of bonding on the underlying aluminum plane	72

List of Tables

3.1	5b/6b encoding	17
3.2	3b/4b encoding	18
3.3	Typical parameters for microstrips on PCBs and flexprints	21
4.1	Some physical properties of aluminum and copper	29
4.2	Calculation of the impedance for coplanar striplines on 25 μm Kapton .	30
4.3	Calculation of the impedance for differential microstrips on 25 μm Kapton	30
4.4	Calculation of the impedance for differential microstrips on 50 μm Kapton	30
4.5	Laser settings used to produce test patterns and flexprints	31
4.6	Laser settings used to produce test patterns and flexprints	32
5.1	Start values of the data generators	47
5.2	Example for an error being counted twice	49
5.3	BERT results for various coplanar striplines	50
5.4	BERT results for various differential microstrips on 25 μm Kapton . . .	50
5.5	BERT results for differential microstrips on 50 μm	50
7.1	Recommended structures sizes for the Mu3e experiment	70

Bibliography

- [1] J. Beringer et al., [Particle Data Group], “*Review of Particle Physics (RPP)*”, Phys.Rev., **D86** 010001, 2012.
- [2] G. Aad et al., [ATLAS Collaboration], “*Observation of a new particle in the search for the Standard Model Higgs boson with the ATLAS detector at the LHC*”, Hyperfine Interact., **214**(1-3) 5–11, 2012, (arXiv:1207.7214 [hep-ex]).
- [3] S. Chatrchyan et al., [CMS Collaboration], “*Observation of a new boson at a mass of 125 GeV with the CMS experiment at the LHC*”, Phys.Lett.B, 2012, (arXiv:1207.7235 [hep-ex]).
- [4] Wikimedia Commons, Standard Model of Elementary Particles, http://en.wikipedia.org/wiki/File:Standard_Model_of_Elementary_Particles.svg, 2014, [Online; accessed 10-Februar-2014].
- [5] Y. Fukuda et al., [Super-Kamiokande Collaboration], “*Evidence for Oscillation of Atmospheric Neutrinos*”, Phys. Rev. Lett., **81** 1562–1567, 1998, (arXiv:hep-ex/9807003).
- [6] Q. R. Ahmad et al., [SNO Collaboration], “*Measurement of the charged current interactions produced by B-8 solar neutrinos at the Sudbury Neutrino Observatory*”, Phys. Rev. Lett., **87** 071301, 2001, (arXiv:nucl-ex/0106015).
- [7] K. Eguchi et al., [KamLAND Collaboration], “*First results from KamLAND: Evidence for reactor anti- neutrino disappearance*”, Phys. Rev. Lett., **90** 021802, 2003, (arXiv:hep-ex/0212021).
- [8] F.P. An et al., [Daya Bay Collaboration], “*Observation of electron-antineutrino disappearance at Daya Bay*”, Phys.Rev.Lett., **108** 171803, 2012, (arXiv:1203.1669 [hep-ex]).
- [9] L. Canetti and M. Shaposhnikov, “*The ν MSM and muon to electron conversion experiments*”, Hyperfine Interact., DOI: 10.1007/s10751-013-0796-7, 2013.
- [10] A. Blondel et al., “*Research Proposal for an Experiment to Search for the Decay $\mu \rightarrow eee$* ”, ArXiv e-prints 1301.6113, January 2013, (arXiv:1301.6113 [physics.ins-det]).
- [11] W. J. Marciano, T. Mori and J. M. Roney, “*Charged Lepton Flavor Violation Experiments*”, Ann.Rev.Nucl.Part.Sci., **58** 315–341, 2008.
- [12] Y. Kuno and Y. Okada, “*Muon Decay and Physics Beyond the Standard Model*”, Rev. Mod. Phys., **73** 151–202, 2001, (arXiv:hep-ph/9909265).

- [13] D. Nicolo, [MEG Collaboration], “*The $\mu \rightarrow e\gamma$ experiment at PSI*”, Nucl.Instrum.Meth., **A503** 287–289, 2003.
- [14] U. Bellgardt et al., [SINDRUM Collaboration], “*Search for the Decay $\mu^+ \rightarrow e^+e^+e^-$* ”, Nucl.Phys., **B299** 1, 1988.
- [15] J. Adam et al., [MEG Collaboration], “*New Constraint on the Existence of the $\mu^+ \rightarrow e^+\gamma$ Decay*”, Phys. Rev. Lett., **110** 201801, May 2013.
- [16] A.M. Baldini et al., “*MEG Upgrade Proposal*”, ArXiv e-prints, January 2013, (arXiv:1301.7225 [physics.ins-det]).
- [17] A. Blondel et al., Letter of intent for an experiment to search for the decay $\mu \rightarrow eee$, 2012.
- [18] M. Kiehn, *Track Fitting with Broken Lines for the MU3E Experiment*, Diploma thesis, Heidelberg University, 2012.
- [19] R. M. Djilkibaev and R. V. Konoplich, “*Rare Muon Decay $\mu^+ \rightarrow e^+e^-e^+\nu_e\bar{\nu}_\mu$* ”, Phys.Rev., **D79** 073004, 2009, (arXiv:0812.1355 [hep-ph]).
- [20] I. Perić et al., “*High-voltage pixel detectors in commercial CMOS technologies for ATLAS, CLIC and Mu3e experiments*”, Nucl.Instrum.Meth., **A731** 131–136, 2013.
- [21] N. Berger et al., “*A Tracker for the Mu3e Experiment based on High-Voltage Monolithic Active Pixel Sensors*”, Nucl. Instr. Meth. A, **732** 61–65, 2013, (arXiv:1309.7896 [physics.ins-det]).
- [22] H. Augustin, *Charakterisierung von HV-MAPS*, Bachelor thesis, Heidelberg University, 2012.
- [23] A.-K. Perrevoort, *Characterisation of High Voltage Monolithic Active Pixel Sensors for the Mu3e Experiment*, Master thesis, Heidelberg University, 2012.
- [24] R. Philipp, *Characterisation of High Voltage Monolithic Active Pixel Sensors for the Mu3e Experiment*, Master thesis, Heidelberg University, 2014.
- [25] C. Grzesik, *Fast Optical Readout for the Mu3e Experiment*, Bachelor thesis, Heidelberg University, 2014.
- [26] S. Corrodi, *Fast Optical Readout of the Mu3e Pixel Detector*, Master thesis, Heidelberg University, ETH Zurich, 2014.
- [27] S. Bachmann et al., The proposed trigger-less TBit/s readout for the Mu3e experiment, In *JINST 9 C01011 doi:10.1088/1748-0221/9/01/C01011*, 2014.
- [28] A. Damyanova, *Development of a Scintillating Fibre Tracker/Time-of-Flight Detector with SiPM Readout for the Mu3e Experiment at PSI*, Master’s thesis, Geneva University, 2013.
- [29] P. Eckert, *In Preparation*, PhD thesis, Kirchhoff Institut für Physik, 2015.

- [30] M. Zimmermann, *Cooling with Gaseous Helium for the Mu3e Experiment*, Bachelor thesis, Heidelberg University, 2012.
- [31] L. Huxold, *Cooling of the Mu3e Pixel Detector*, Bachelor thesis, Heidelberg University, 2012.
- [32] A. Herkert, *In Preparation*, Master thesis, Heidelberg University, 2015.
- [33] G.S. Bauer, Y. Dai and W. Wagner, “*SINQ layout, operation, applications and R&D to high power*”, J. Phys. IV France, **12**(8) 3–26, 2002.
- [34] A. P. Clark, *Principle of Digital Data Transmission*. Wiley, 1983.
- [35] G. Cariolaro, *Unified signal theory*. London : Springer, 2011.
- [36] M. Werner, *Signale und Systeme*, volume 3. Vieweg+Teubner, 2008.
- [37] H. Zimmermann, “*OSI Reference Model - The ISO Model of Architecture for Open Systems Interconnection*”, IEEE Transactions on Communications, **28**(4) 425–432, 1980.
- [38] Wikimedia Commons, Low-Voltage Differential Signaling, <http://en.wikipedia.org/wiki/LVDS>, 2014, [Online; accessed 12-August-2014].
- [39] <http://www.maximintegrated.com/en/app-notes/index.mvp/id/3662>, Understanding LVDS Fail-Safe Circuits, 2014, [Online; accessed 11-August-2014].
- [40] M. Pauer, *Return-to-zero Coding in Optical Intersatellite Links*. Technische Universität Wien, 2003.
- [41] Wikimedia Commons, Leitungscode, <http://de.wikipedia.org/wiki/Leitungscode>, 2014, [Online; accessed 12-August-2014].
- [42] R. Forster, “*Manchester encoding: Opposing definitions resolved*”, Engineering Science & Education Journal, 2000.
- [43] D. Derickson and M. Müller, *Digital Communications Test and Measurement: High-Speed Physical Layer Characterization*. Prentice Hall, December 2007.
- [44] A. X. Widmer and P. A. Franaszek, “*A DC-Balanced, Partitioned-Block, 8B/10B Transmission Code*”, IBM Journal of Research and Development, **27**(5) 440, 1983.
- [45] Wikimedia Commons, Ersatzschaltbild eines kurzen Stückes einer Zweidrahtleitung, <http://de.wikipedia.org/wiki/Leitungstheorie#mediaviewer/Datei:Leitungsbelag.svg>, 2014, [Online; accessed 11-August-2014].
- [46] M. Johnson and W. Graham, *High-Speed Signal Propagation*. Prentice Hall PTR, 2003.
- [47] E. Bogatin, Training for signal integrity and interconnect design, <http://www.ewh.ieee.org/r5/denver/rockymountainmc/archive/2000/diffimp.pdf>, 2000.

- [48] D. Brooks, “*Differential Impedance - What’s the Difference?*”, Printed Circuit Design, 1998.
- [49] P. Vielhauer, *Theorie der Übertragung auf elektrischen Leitungen*. Verlag Technik, 1970.
- [50] D. Brooks, *Printed Circuit Board Design*. Prentice Hall PTR, 2003.
- [51] S. Gevorgian and H. Berg, “*Line Capacitance and Impedance of Coplanar-Strip Waveguides on Substrate with Multiple Dielectric Layers*”, IEEE Xplore, year unknown.
- [52] Würth Elektronik, *Basic Design Guide*, 2012, http://www.wedirekt.de/web/live/media/16_wedirekt/spezifikationen/leiterplatten_daten_downloads/WEdirektBasicDesignGuide.pdf.
- [53] Dyconex, *Design Guide 2013 (External)*, 2013, Available on request via e-mail.
- [54] T. Hebbeker, “*Calculating Upper Limits with Poisson Statistics*”, <http://web.physik.rwth-aachen.de/~hebbeker/l3note-2633.pdf>, 2001.
- [55] I. Narsky, “*Estimation of Upper Limits Using a Poisson Statistic*”, arXiv:hep-ex/9904025, page 24, 1999.
- [56] ON Semiconductor, “*Understanding Data Eye Diagram Methodology for Analysing High Speed Digital Signals*”, Semiconductor Components Industries, LLC, **AND9075/D**, 2014.
- [57] <http://uniquelaserengravers.tradeindia.com/pl6mw-1118929.html>, [Online; accessed 20-August-2014].
- [58] Universal Laser Systems, *PLS User Guide*, 2012.
- [59] DuPont, *Kapton[®] HN polyimide film - Technical Data Sheet*, 2011.
- [60] DuPont, *Kapton[®] HN - Summary of Properties*, year unknown.
- [61] M. Baucio, *ASM Metals Reference Book*. ASM International, 1993.
- [62] <http://www.aluinfo.de/index.php/aluminium-in-electrical-engineering-and-electronics.html>, [Online; accessed 20-August-2014].
- [63] Los Alamos National Laboratory, <http://periodic.lanl.gov/13.shtml>, [Online; accessed 20-August-2014].
- [64] S. Eidelman et al., “*Passage of Particles Through Matter*”, Physics Letters B592, 2004.
- [65] J. Bartl and M. Baranek, “*Emissivity of Aluminum and its Importance for Radiometric Measurements*”, Measurement Science Review, 2004.
- [66] Y. Kaburagi and Y. Hishiyama, “*Ferromagnetism discovered on heat-treating the aromatic polyimide film Kapton*”, J. Mater. Res., 2002.

- [67] Altera, *Stratix V Device Handbook*, 2013.
- [68] W. Rogers et al., *FPGA-based Implementation of Signal Processing Systems*. Wiley, 2008.
- [69] Altera, *Stratix V Device Overview*, 2014.
- [70] Altera, *Stratix V GX FPGA Development Board - Reference Manual*, 2014.
- [71] <http://www.altera.com/products/devkits/altera/kit-sv-gx-host.html>, [Online; accessed 21-August-2014].
- [72] Altera, *High Speed Mezzanine Card (HSMC) - Specification*, 2009.
- [73] Altera, *Quartus II Handbook Volume 1: Design and Synthesis*, 2014.
- [74] V. A. Pedroni, *Circuit Design with VHDL*. MIT Press, 2004.
- [75] S. Palnitkar, *Verilog HDL: A Guide to Digital Design and Synthesis*. Prentice Hall PTR, 2003.
- [76] ModelSim SE, *User's Manual*, 2002.
- [77] Ken Boyette, http://read.pudn.com/downloads104/sourcecode/embed/425959/8b_10b/8b10_enc.vhd__.htm, 2006, [Online; accessed 25-April-2014].
- [78] Ken Boyette, http://read.pudn.com/downloads104/sourcecode/embed/425959/8b_10b/8b10_dec.vhd__.htm, 2006, [Online; accessed 25-April-2014].
- [79] Tektronix, *Digital-Phosphor-Oszilloskope - DPO7000C-Serie Datenblatt*, 2013.
- [80] Altera, *DPO7000 Series - Digital Phosphor Oscilloscopes - Quick Start User Manual*.
- [81] Tektronix, *Differential Probes - TDP1500 and TDP3500 Datasheet*, 2013.
- [82] I. Peric, Personal Contact, September 2014.

Acknowledgements

At the end of my thesis, I would like to thank everyone who supported me to carry out this thesis.

First of all, I would like to express my appreciation to **Prof. Dr. André Schöning** who gave me the opportunity to work in the Mu3e group. He helped me especially by critically questioning my strategies and supposing new approaches.

I would also like to thank **Prof. Dr. Ulrich Uwer** for being my second examiner.

Moreover, I would like to express my gratitude to the following persons in no specific order:

- **Carsten Grzesik**, with whom I have spent much time in the lab and at the laser platform. I also profited a lot from his experience.
- **Qinhua Huang**, who taught me much about VHDL and supported me on FPGA programming.
- **Dirk Wiedner**, who gave me valuable support on technical and electronic issues and helped me to design my HSMC Flexprint Adapter Board.
- **Niklaus Berger**, who is an expert in FPGA programming and was able to solve every problem Qinhua and I were facing.
- **Ann-Kathrin Perrevoort** and all the others who were always there to answer questions, proof-read my thesis with great commitment and gave a lot of suggestions.
- Finally, the whole **Mu3e group** for providing a very pleasant and cordial work atmosphere and sharing a time full of new experiences.

Erklärung

Ich versichere, dass ich diese Arbeit selbstständig verfasst und keine anderen als die angegebenen Quellen und Hilfsmittel benutzt habe.

Heidelberg, den 15.09.2014